Synchronizing Geomagnetic Field Intensity Records in the Levant Between the 23rd and 15th Centuries BCE: Chronological and Methodological Implications

Ron Shaar, Shlomit Bechar, Israel Finkelstein, Yves Gallet, Mario A. S. Martin, Yael Ebert, Jonathan Keinan, Lilach Gonen

Geochemistry, Geophysics, Geosystems

RESEARCH ARTICLE
10.1029/2020GC009251

Key Points:

- Archeointensity compilation of the Levant and western Upper Mesopotamia based on synchronized datasets from Mari, Ebla, Hazor, and Megiddo
- Compatibility of paleointensity data was verified through a blind test of the Triaxe versus the Thellier-IZZI-MagIC methods
- Synchronization of the archeological timescale was achieved by linking the data to radiocarbon ages from Megiddo

Supporting Information:

- Supporting Information S1
- Table S1
- Table S2
- Table S3

Correspondence to:
R. Shaar,
ron.shaar@mail.huji.ac.il

Citation:
Shaar, R., Bechar, S., Finkelstein, I., Gallet, Y., Martin, M. A. S., Ebert, Y., et al. (2020). Synchronizing geomagnetic field intensity records in the Levant between the 23rd and 15th centuries BCE: Chronological and methodological implications. *Geochemistry, Geophysics, Geosystems*, *21*, e2020GC009251. https://doi.org/10.1029/2020GC009251

Received 16 JUN 2020
Accepted 31 OCT 2020

Synchronizing Geomagnetic Field Intensity Records in the Levant Between the 23rd and 15th Centuries BCE: Chronological and Methodological Implications

Ron Shaar[1], Shlomit Bechar[2,3], Israel Finkelstein[4], Yves Gallet[5], Mario A. S. Martin[4], Yael Ebert[1], Jonathan Keinan[1], and Lilach Gonen[1]

[1]The Institute of Earth Sciences, The Hebrew University of Jerusalem, Jerusalem, Israel, [2]The Institute of Archaeology, The Hebrew University of Jerusalem, Jerusalem, Israel, [3]The Haifa Center for Mediterranean History, University of Haifa, Haifa, Israel, [4]The Sonia and Marco Nadler Institute of Archaeology, Tel Aviv University, Tel Aviv, Israel, [5]Université de Paris, Institut de Physique du Globe de Paris, CNRS, Paris, France

Abstract Archeomagnetic records are an important source of information on the past behavior of the geomagnetic field. Frequently, however, coeval archeomagnetic intensity (archeointensity) datasets from nearby locations display significant discrepancies, hampering precise reconstruction of high-resolution secular variation curve. This is the case for the time interval between the later phase of the Early Bronze and the early phase of the Late Bronze Ages (23rd–15th centuries BCE) in the Levant and Mesopotamia. We address the problem by cross-correlating archeointensity datasets from four major multilayered archeological sites in the southern Levant (Hazor and Megiddo), northern Levant (Ebla), and western Upper Mesopotamia (Mari). We report new archeointensity data, obtained using the Thellier-IZZI-MagIC and the Triaxe methods, from six strata at Hazor and four radiocarbon-dated strata at Megiddo. From 39 pottery fragments, 199 specimens passed our selection criteria, from which we calculated the mean archeointensity for each stratum. To strengthen the comparison of these data with previously published data from Mari and Ebla, obtained using the Triaxe method, we conducted a blind test of the methods that resulted in indistinguishable results or a difference of less than 1 μT. The synchronized compilation, constrained by radiocarbon data from Megiddo, displays a V-shaped pattern with a prominent minimum of at least 200 years centered around the 18th century BCE. The study highlights the importance of stacking archeomagnetic data obtained by different archeointensity methods only after cross-testing the methods and ensuring that archeological samples were dated in a consistent manner.

Plain Language Summary Archeological materials heated to high temperatures, such as pottery, can act as recorders of the ancient geomagnetic field and may provide invaluable information on its behavior through time. With the advance of paleomagnetic techniques, geophysicists can recover, with greater precision than ever, the absolute intensity of the geomagnetic field at the time when an archeological artifact was heated. However, archeological uncertainty often hampers the possibility of precisely dating these materials. This poses a challenge to both archeologists and paleomagnetists. In this paper, we demonstrate a cross-disciplinary collaboration which sheds light on fundamental problems regarding the Ancient Near East in the Bronze Age. The underlying principle of the method is that contemporaneous ceramics from nearby archeological sites must have recorded the same field intensity. We use this approach to synchronize archeomagnetic intensity records of four major Bronze Age sites in the Levant and Mesopotamia: Hazor, Megiddo, Ebla, and Mari. We tie the combined record to radiocarbon ages from five strata at Megiddo. The intensity-synchronized compilation depicts fast changes in the ancient field intensity, which illuminates some long-standing chronological disputes regarding the history of the Ancient Near East.

1. Introduction

Regional and global geomagnetic models of the Holocene, which describe the time evolution of the geomagnetic field vector, are of interest to a number of research fields, including exploration of the geodynamo (Davies & Constable, 2017; Korte et al., 2011; Livermore et al., 2014) and archeomagnetic dating (Gallet et al., 2014b, 2020; Hervé & Lanos, 2018; Peters et al., 2018; Stillinger et al., 2016). As a result, considerable

effort has been invested over the past decades in improving the resolution, accuracy, and coverage of geomagnetic models (Arneitz et al., 2019; Campuzano et al., 2019; Hellio & Gillet, 2018; Korte et al., 2011; Nilsson et al., 2014; Osete et al., 2020; Pavón-Carrasco et al., 2014), leading to a growing need for high-quality Holocene paleomagnetic records. Archeomagnetic data of the past several millennia, derived from the analysis of well-dated baked clay artifacts, are significant in this effort because they enable recovery of the absolute intensity of the ancient field (*archeointensity*). One of the main challenges in this respect is synchronizing archeomagnetic datasets obtained from different archeological sites, because frequently, coeval records from the nearby locations display significant discrepancies. This is a result of biases both in age scales and archeointensity determinations. Age biases can, for example, result from stratigraphic uncertainties, usage of different terminologies for archeological periods, and limited quantity of radiocarbon data. Archeointensity biases can be caused by inconsistency in paleointensity methods and laboratory protocols, selection criteria, and averaging schemes.

The archeointensity data from Turkey, Syria, Jordan, Cyprus, and Israel, published over the past decades (Ben-Yosef et al., 2017; Ben-Yosef et al., 2008, 2009; Ertepinar et al., 2012, 2016, 2020; Gallet et al., 2006, 2008, 2014a, 2015, 2020; Gallet & Al-Maqdissi, 2010; Gallet & Butterlin, 2015; Gallet & Le Goff, 2006; Genevey et al., 2003; Shaar et al., 2011, 2015, 2016; Stillinger et al., 2015) potentially provide sufficient information to inspect the behavior of the field in this region with an improved resolution and accuracy. Yet, when these recent data are plotted together with all other data published since the 1980s, substantial discrepancies arise (Figure S1). The noise in this compilation can be attributed to large variabilities in dating approaches, laboratory methods, and interpretation techniques.

As part of our efforts to construct a detailed and consistent archeointensity database for the Levant, we focus in this study on the time interval between 2300 and 1400 BCE. Gallet et al. (2014a) suggested that field behavior during this period is characterized by a V-shaped pattern, with a minimum during the 19th and 18th centuries BCE, which marks the lowest field in the Levant during the past 4,500 years. This unique trend falls with several key historical events that make the archeointensity curve important for both archeomagnetic dating and geomagnetic secular variation research. Figure 1 shows archeointensity data within this time interval obtained using only modern paleointensity standards (Ertepinar et al., 2016, 2020; Gallet & Le Goff, 2006; Gallet et al., 2006, 2008, 2014a; Genevey et al., 2003; Shaar et al., 2016; Stillinger et al., 2015). Older datasets, which do not include corrections for both anisotropy and cooling rate effects (Athavale, 1969; Games, 1980; Hussain, 1983; Odah, 1999, 2004; Odah et al., 1995), are not shown. The significance of these corrections has been well known for decades (Fox & Aitken, 1980; Rogers et al., 1979) and we further demonstrate it in Section 3. In addition, Figure 1 ignores a dataset published without details on quality criteria (Aitken et al., 1984), which prevents comparison with modern data. The compilation shown in Figure 1 displays significant inconsistencies hindering attempts to construct precise high-resolution secular variation curve. Distinguishing between discrepancies resulting from archeological uncertainties or age biases and those resulting from archeointensity methodological issues is not trivial. From a dating viewpoint, only few sites are radiocarbon dated (Kültepe, Kinet Höyük, Tel Atchana, and Tel Megiddo [Figure 1a]); archeological dating of the other sites relies on different, and sometime contradicting, archeochronological frameworks (e.g., Figure S2). From an archeointensity perspective, the different datasets were obtained using a range of methods (several variants of the Thellier method applied using different selection criteria, Triaxe, and microwave) and different averaging and error estimation schemes. Thus, compatibility between the archeointensity values in the compilation shown in Figure 1 may be questionable without rigorous testing.

The purpose of this study is to minimize the noise in the archeointensity picture displayed in Figure 1. Our approach is as follows: first, we establish compatibility between data obtained using the Triaxe and the Thellier-IZZI-MagIC methods (see Section 2.2 for methods) in a "blind test." This is done because, for this paper, the majority of the data was obtained using these two methods. Then, we report new data for pottery collected from four radiocarbon-dated strata in Tel Megiddo and six archeologically dated strata in Tel Hazor (Israel, Figure 1a). Under a working assumption that contemporaneous ceramics from nearby archeological sites must have recorded the same field intensity, we assemble a reduced synchronized dataset, constrained by Tel Megiddo radiocarbon ages. The synchronized dataset is based on data from four major multilayered archeological sites studied using paleointensity methods that were tested against each

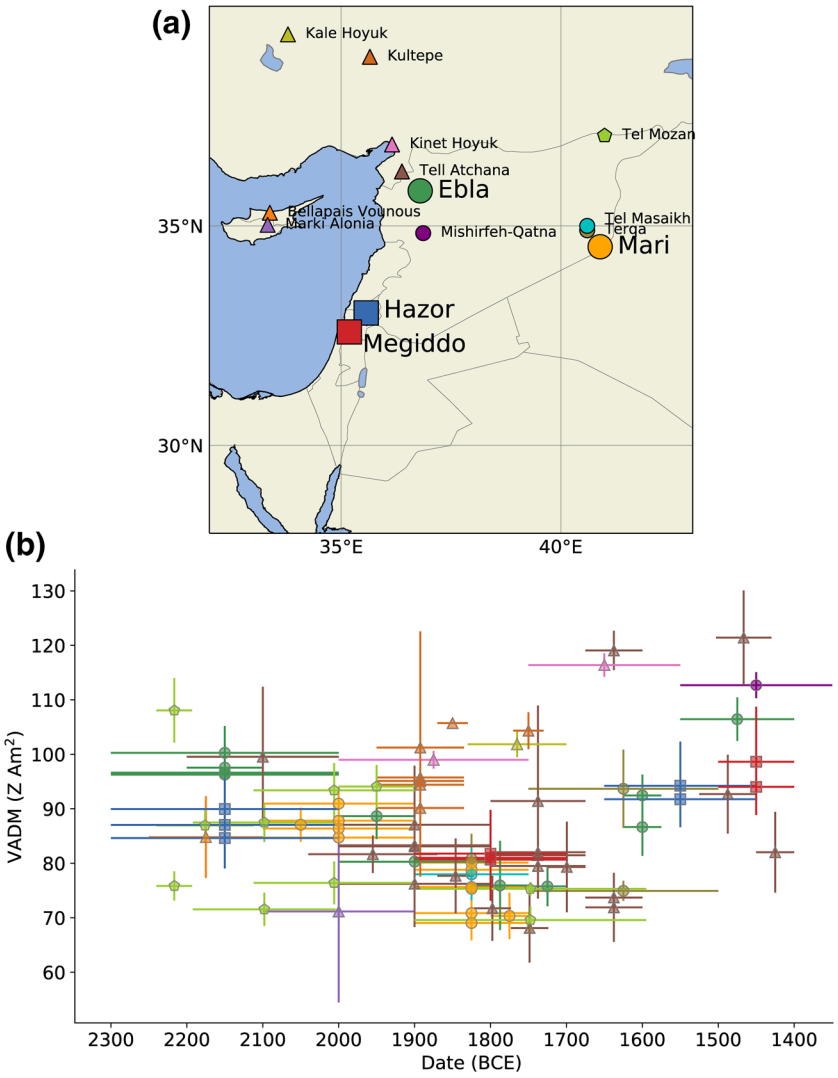

Figure 1. Published archeointensity data from the Levant and western Upper Mesopotamia. (a) Location map. (b) Archeointensity expressed as virtual axial dipole moment (VADM). Symbols denote for archeointensity methods and selection criteria. See text for the difference between the protocols. Squares: Thellier-IZZI-MagIC (Shaar et al., 2016); circles: Triaxe and/or Thellier-Coe tested against Triaxe (Gallet et al., 2006, 2008, 2014a; Gallet & Al-Maqdissi, 2010; Gallet & Le Goff, 2006; Genevey et al., 2003); triangles: microwave (Ertepinar et al., 2020) or microwave combined with Thellier-Type and multispecimen (Ertepinar et al., 2016); pentagons: Thellier-IZZI (Stillinger et al., 2015).

other: Tel Hazor and Tel Megiddo (Israel), Ebla (Tell Mardikh, Syria, in the northern Levant), and Mari (Tell Hariri, Syria, in western Upper Mesopotamia) (Figure 1a). Finally, we compare the reduced synchronized compilation with other sites, which were analyzed using methods that were not tested against Thellier-IZ-ZI-MagIC and/or Triaxe.

2. Materials and Methods

2.1. Archeological Sampling

2.1.1. Tel Hazor

Tel Hazor (33.017°N, 35.568°E) is one of the largest tel sites in the southern Levant. It was the most important Canaanite urban center in the region in the second millennium BCE and continued to be a significant city in the Iron Age. The first excavations of Tel Hazor were conducted in the 1950s and 1960s by the late

Yigael Yadin. Excavations were renewed by Amnon Ben-Tor in 1990. Both excavations were carried out under the auspices of the Hebrew University of Jerusalem. Directors of the current dig are Amnon Ben-Tor and Shlomit Bechar. Tel Hazor is composed of a sequence of more than 20 strata that span from the Early Bronze to the Persian period (ca. 30th–4th centuries BCE), representing a nearly continuous occupation. Hazor was first established as a large urban center in the Middle Bronze (Figure S2). The Middle Bronze city encompassed an area of approximately 84 hectares – in both the acropolis and lower city – with temples, residential quarters, workshops, a palace, and open cultic places (for an extensive description of the site and its monuments, see Ben-Tor [2015] and Yadin [1972]). Two strata are attributed to the Middle Bronze: XVII and XVI in the acropolis and 4 and 3 in the lower city. In this study, we also consider Stratum XV, which begins at the end of the Middle Bronze III and continues to the Late Bronze I, and Stratum XVIII, which represents a rural settlement of the Early Bronze IV (ca. 2350–2000 BCE) (this period is termed Intermediate Bronze Age by many of the scholars studying the southern Levant). For archeointensity analysis, we collected pottery vessels, with emphasis on local domestic material, from a succession of six stages in Strata XVII–XVI in the acropolis, based on architectural and ceramic considerations (Ben-Tor et al., 2017). These stages, labeled from top to bottom – XVI-A, XVI-B, XVI-C, XVII-D, XVII-E, and XVII-F – were exposed in an open cultic area near the entrance to the palace. Their initial ages are assigned following Ben-Tor (2004), who dated the establishment of MB Hazor (i.e., the beginning of Stratum XVII) to 1720–1710 BCE, the beginning of its peak (Stratum XVI) to around 1680 BCE, and its end to 1550 BCE. The ages assigned by Ben-Tor (2004) follow the Mesopotamian "Ultra Low Chronology" (Figure S2). Archeological information on each of the investigated artifacts is provided in the supporting information.

2.1.2. Tel Megiddo

Megiddo (32.585°N, 35.185°E) is the type site for the Bronze and Iron Ages in the southern Levant. It was the hub of a city-state in the Bronze Age and an important administration center of the Northern Kingdom (Israel) in the Iron Age. The site was excavated by a German expedition in the early 20th century and a University of Chicago team in the 1920s and 1930s. Yigael Yadin of the Hebrew University of Jerusalem carried out soundings at Megiddo in the 1960s and early 1970s. The site has been excavated by a team from Tel Aviv University since 1994; the directors of the current dig are Israel Finkelstein, Mario A.S. Martin, and Matthew J. Adams. Megiddo was continuously inhabited from the PrePottery Neolithic to the Persian period (ca. 10,000–333 BCE). Excavations revealed a dense stratigraphic sequence of over 30 settlements. Bronze Age Megiddo features impressive remains of fortifications (including gates), palaces, and temples (for the site, history of excavations, and main monuments, see Ussishkin [2018]). The current excavation focuses on tight control over stratigraphy and ceramic typology and on a rigorous program of radiocarbon dating. The latter, with an unprecedented number of samples, encompasses almost the entire stratigraphic sequence; special attention was taken to process only samples that originate from secure stratigraphic contexts: Regev et al. (2014) for the Early Bronze; Martin et al. (2020) for the later phases of the Middle Bronze and the Late Bronze; Toffolo et al. (2014) for the Iron Age. For the present study, we collected pottery samples from four layers: (1) Level S-2 – a destruction level from the early days of the Middle Bronze I unearthed on the northern slope of the mound, near its gate; preliminary analysis of radiocarbon ages of burnt material suggests an age range of ca. 1950–1900 BCE. (2, 3) Levels K-11 and K-10 of the Middle Bronze III in the southeastern sector of the site. (4) Level H-15 of the Late Bronze I in the northwestern sector of the site. The age spans of K-11 (ca. 1650–1600), K-10 (ca. 1600–1550), and H-15 (ca. 1550–1475) were calculated according to the Bayesian age model of Martin et al. (2020). Collection of the pottery samples was done with emphasis on local domestic material securely associated with stratigraphic and ceramic context and thus with radiocarbon dates.

2.2. Archeointensity Methods

Our reduced dataset is based on three methods, which were tested against each other and show compatibility: (1) the Thellier method (Thellier & Thellier, 1959) applied using the IZZI protocol (Tauxe & Staudigel, 2004; Yu et al., 2004) and analyzed using the automatic interpretation technique of Shaar and Tauxe (2013) with criteria defined in Shaar et al. (2016), hereafter called Thellier-IZZI-MagIC (squares in Figure 1) (Shaar et al., 2016); (2) the Thellier method applied using the Coe protocol (Coe, 1967), hereafter termed Thellier-Coe (circles in Figure 1) with the criteria of Genevey et al. (2003); and (3) the Triaxe method

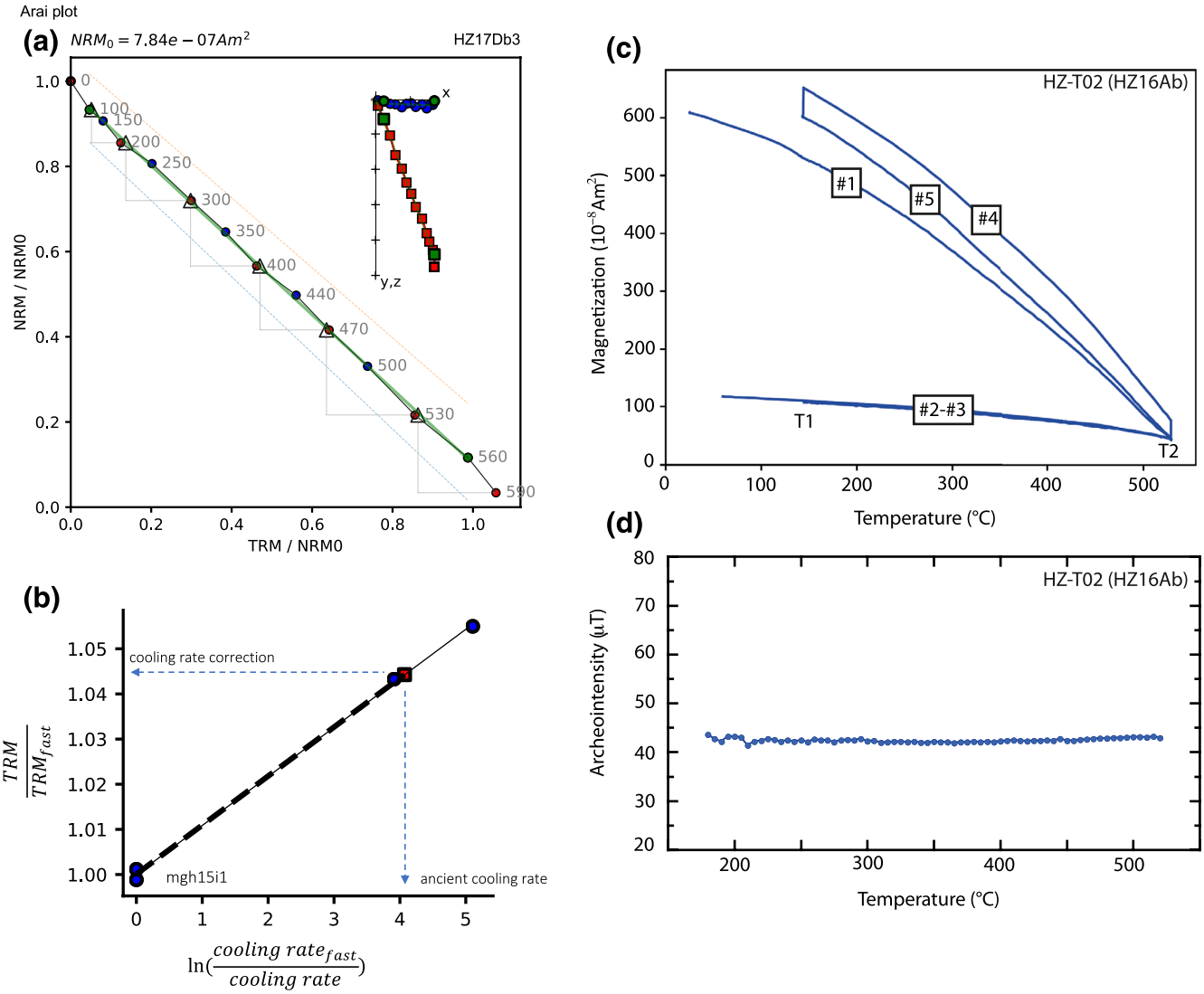

Figure 2. Archeointensity methods. (a) Representative Arai diagram and Zijderveld plot (inset) displaying ideal linear behaviors in the Thellier-IZZI experiments. (b) Cooling rate experiment, where circles show four laboratory thermoremanent magnetizations (TRMs) acquired under different cooling rates, solid line shows best fit line through points, and red square shows the projection of the ancient cooling rate on the best fit line. (c and d) Representative results from a Triaxe experiment.

(Le Goff & Gallet, 2004) (circles in Figure 1) (Gallet et al., 2006, 2008, 2014a; Gallet & Le Goff, 2006). In the following, we review the main concepts of each method and assess the differences between them. In Section 3.1, we provide the experimental evidence for compatibility.

2.2.1. Thellier-IZZI-MagIC

Thellier-IZZI-MagIC archeointensity experiments of samples collected for this study were carried out in the shielded paleomagnetic laboratory at the Institute of Earth Sciences, The Hebrew University of Jerusalem (HUJI), using modified ASC TD-48 ovens, 2G-750 superconducting rock magnetometer (SRM), and 2G-RAPID SRM. We cut several specimens from each pottery fragment (sample) and glued them inside nonmagnetic glass vials of 12 mm in diameter (Hazor samples), or in 22 mm × 22 mm × 20 mm square alumina crucibles (Megiddo samples). Archeointensity experiments followed the IZZI protocol (Tauxe & Staudigel, 2004; Yu et al., 2004) with routine pTRM checks at every second temperature step (Coe et al., 1978), using an oven field of 40 or 50 μT. Heating time ranged from 40 to 65 min depending on the target temperature. Figure 3a shows typical successful data from these experiments, with Arai plot (Nagata

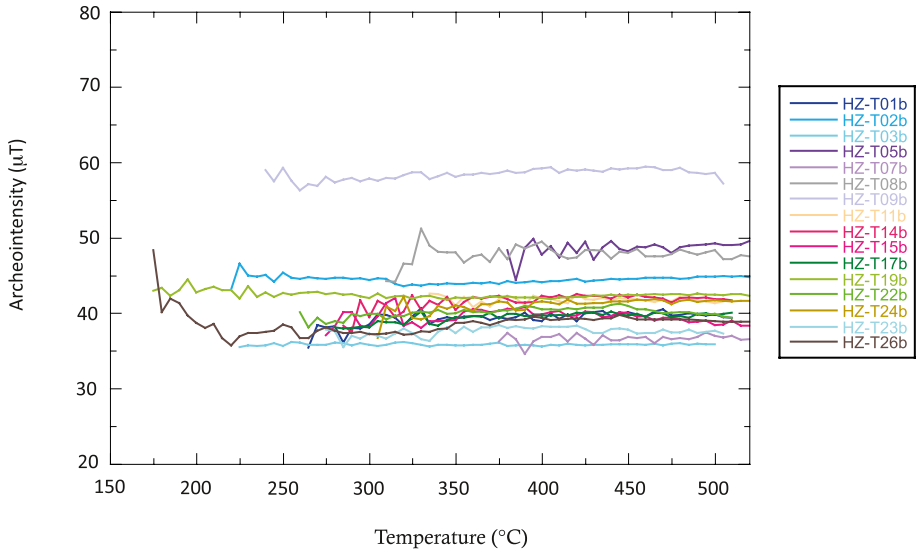

Figure 3. Triaxe archeointensity (*R*') curves for one specimen per sample ("b" specimen). Only samples passing the acceptance criteria in Table 2 are shown.

et al., 1963) displaying a linear behavior, successful pTRM check (graphically displayed as triangles overlapping the IZZI datapoints), and a stable straight single-component Zijderveld diagram (Zijderveld, 1967) converging to the origin.

Anisotropy of thermoremanent magnetization (ATRM) experiments consisted of eight heating steps carried out at the highest temperature that the specimens reached during the Thellier experiment: a baseline step in a zero field (subtracted from the subsequent infield measurements), six infield steps at orthogonal directions (+x, +y, +z, −x, −y, −z) in 40 or 50 μT, and an additional infield alteration check at the end of the experiment. As the long, repeated high-temperature procedures can cause alteration of the magnetic minerals, we calculated an alteration parameter from the vector differences of four pairs of measurements: ([−x, +x], [−y, +y], [−z, +z], and [first measurement, alteration-check measurement]). ATRM data of specimens with alteration check >6% were rejected. For these specimens, anisotropy was measured using anhysteretic remanent magnetization (ARM) acquired at 100-mT AC field and 0.1-mT DC bias field at six orthogonal directions, similar to the ATRM experiment, where AF demagnetization step at 110 mT was applied before each ARM step. AARM experiments were carried out after thermal demagnetization of the specimens. Anisotropy tensors were calculated following Hext (1963), using the PmagPy Thellier GUI program (Shaar & Tauxe, 2013; Tauxe et al., 2016).

Cooling rate correction experiments consisted of 4–5 cooling steps from 590°C or 600°C to room temperature: a baseline zero-field step, an in-field step in a fast (regular) cooling rate, one or two in-field steps at slower cooling rate, and finally, an in-field alteration check step in a fast cooling rate. Cooling rate alteration parameter was calculated as the percentage of difference between the first and the last cooling steps. Specimens with alteration parameter >6% were rejected, and their cooling rate correction factor was calculated by averaging the correction factors of sister specimens from the same mother fragment. Cooling rate correction factors were calculated using the PmagPy Thellier-GUI program, assuming a logarithmic relation between $\frac{TRM}{TRM_{\text{oven}}}$ and $\frac{Cooling\ rate}{Cooling\ rate_{\text{oven}}}$ (Genevey & Gallet, 2002; Halgedahl et al., 1980). Correction factors were calculated from the best fit line through the experimental cooling rate data, as illustrated graphically in Figure 2b. In our calculation, we assumed an averaged ancient cooling rate of 6 h from 500°C to 200°C for all specimens following Genevey et al. (2003) and Shaar et al. (2016).

Archeointensity values were calculated with the *Thellier-GUI* program (Shaar & Tauxe, 2013), incorporated into the *PmagPy* software package (Tauxe et al., 2016), using the *Thellier Auto Interpreter* algorithm, and the acceptance criteria listed in Table 1. The Thellier Auto Interpreter performs the following tasks:

Table 1
Acceptance Criteria Applied to the Thellier-IZZI-MagIC Data

Criteria group	Statistic	Threshold value	Description	Reference[b]
Specimen paleointensity[a]	FRAC	0.79	Fraction parameter	[1]
	β	0.1	Scatter parameter	[2], [3]
	SCAT	True	Scatter parameter	[1]
	N_{PTRM}	2	Number of pTRM checks	
	n	4	Number of data points	
	MAD	5	Maximum angular deviation of the zero field steps	[4]
	DANG	10	Deviation angle	[5]
	Alteration check (correction)	6%	Alteration check in TRM anisotropy and cooling rate experiments	
Sample(fragment)/site (stratum) paleointensity	N_{min}	3	Number of specimens	
	$N_{min\_aniso\_corr}$	At least half of the specimens	Minimum number of specimens with anisotropy correction	
	$N_{min\_cr\_corr}$	1	Minimum number of specimens with cooling rate correction	
	σ	$\sigma < 3$ μT OR $\sigma\% < 8\%$	Standard deviation of the sample mean	
	Anisotropy sample test	6%	If the mean anisotropy correction of all the specimens from the same sample (fragment) is higher than this value, specimens without anisotropy correction are discarded	

Abbreviation: TRM, thermoremanent magnetization.
[a]For a complete description and definitions, see Paterson et al. (2014) (http://www.paleomag.net/SPD/). [b][1] Shaar and Tauxe (2013); [2] Coe et al. (1978); [3]: Selkin and Tauxe (2000); [4]: Kirschvink (1980); [5] Tauxe and Staudigel (2004).

1. Line fitting to the Arai plot: The program analyzes all the possible best fit lines of each Arai plot separately and filters out the interpretations (best fit lines) that fail the specimen acceptance criteria
2. Applying corrections: Each interpretation that passes step 1 is corrected for the effect of anisotropy and cooling rate
3. Sample/site mean calculation: The program calculates all the possible sample/site means (where sample denotes for a pottery fragment, and site is attributed to archeological stratum, level, or context) using all the specimens' acceptable interpretations calculated in steps 1 and 2. Means that fail the sample/site acceptance criteria in Table 1 are screened out
4. STDEV-OPT sample/site mean calculation: From all the acceptable sample/site means calculated in step 3, the STDEV-OPT (standard deviation optimum) mean is the mean that has the lowest coefficient of variation statistic ($\sigma_{\%} = 100 \times [\sigma/\text{mean}]$, where σ is the standard deviation)
5. Calculating error bounds: Uncertainty bounds are defined by taking from all the acceptable means calculated in step 3, the two end-case interpretations with the lowest and the highest values, and adding or subtracting from them the standard deviation (these end case values are $[B_{min} - \sigma_{max}]$ and $[B_{max} + \sigma_{max}]$)

2.2.2. Triaxe

Triaxe measurements were done at the paleomagnetic laboratory of the Institut de Physique du Globe de Paris (IPGP) using a Triaxe three-axis vibrating sample magnetometer, which allows magnetization

Table 2
Selection Criteria Applied to the Triaxe Archeointensity Determinations

Criteria level	Criterion group	Description
Specimen	Thermal demagnetization diagram	Univectorial primary TRM
	"$R(T_i)$ data" versus "Temperature" diagram	The $R(T_i)$ values must be continuously increasing or ~constant from T_1 (or T'_1) to T_2.
	"$R'(T_i)$ data" versus "Temperature" diagram	The $R'(T_i)$ values must be sufficiently flat.
		The slope in the diagram, expressed in % through the temperature of analysis must be less than 10% (slope defined by : (R'(T2)-R'(T_1 or T_1'))/(mean $R'(T_i)$ data).
		For mean computation of the $R'(T_i)$ values: The magnetization fraction, with unblocking temperatures larger than T_1(or T_1'), must be at least 50%.
Fragment	Coherence of the intensity values	Results obtained from at least two different specimens.
		Estimated error ≤5% of the corresponding mean.

Abbreviation: TRM, thermoremanent magnetization.

measurements at high temperatures. The experimental protocol is illustrated in Figure 2c, and it includes five heating/cooling steps between two reference temperatures T_1 (generally 150°C) and T_2 (around 500°C): the first (heating) step is natural remanent magnetization (NRM) demagnetization up to T_2; the next two demagnetization steps (cooling-heating) are designed to scrutinize the thermal variation between T_1 and T_2 of the magnetization fraction still unblocked at T_2; the fourth (cooling) is done in a laboratory field whose direction is automatically adjusted so that it leads to the acquisition of laboratory TRM (TRM_{lab}) parallel to the NRM; the fifth (heating) step demagnetizes the latter up to T_2. The intensity value is estimated for each running temperature T_i (every ~5°C) between T_1 and T_2 from the ratio $R'(T_i) = B_{lab}\frac{\left[M_1(T_1) - M_1(T_i)\right] - \left[M_3(T_1) - M_3(T_i)\right]}{\left[M_5(T_1) - M_5(T_i)\right] - \left[M_3(T_1) - M_3(T_i)\right]}$ (Figure 2d), where M_1, M_3, and M_5 are moment measurements at the first, third, and fifth steps (i.e., while temperatures are increasing). If the $R'(T_i)$ data display a straight and flat line, B_{anc} is calculated at the specimen level by averaging all $R'(T_i)$ values, provided that (1) the TRM_{anc} exhibits a single directional component, being that acquired during the manufacture of the artifacts. In case of a secondary magnetization, the pivotal temperature T_1 can be shifted to a higher temperature T_1'; (2) the magnetization isolated between T_1/T_1' and T_2 represents more than 50% of the magnetization fraction remaining above T_1/T_1'. As the direction of TRM_{lab} is parallel to that of NRM, no anisotropy correction on TRM acquisition is required. Furthermore, it was experimentally shown that the cooling rate effect is overcome by considering the $R'(T_i)$ data (Le Goff & Gallet, 2004). For an in-depth review on the method and the selection criteria, see Le Goff and Gallet (2004), Genevey et al. (2009), and Hartmann et al. (2010). Table 2 lists the selection criteria of the Triaxe method (see also Gallet et al., 2020).

3. Results

3.1. Blind Test of the Methods

As the motivation for this study is synchronizing archeointensity datasets acquired using different laboratory procedures, we performed a "blind test" aimed at assessing the compatibility between the Thellier-IZZI-MagIC and Triaxe methods. Gallet and Le Goff (2006) already compared archeointensity data from Syria obtained using the Triaxe and the Thellier-Coe methods (additional comparisons were also carried out by Genevey et al. [2009], Hartmann et al. [2010], Hartmann et al. [2011], and Hervé et al. [2017]). They concluded that when using the selection criteria in those studies, the two methods yield equivalent data. The Thellier-IZZI-MagIC applied here adopts an automatic interpretation procedure with different acceptance criteria than in Gallet and Le Goff (2006) and Genevey et al. (2003). Hence, we augment their conclusions with additional testing of the Triaxe with the Thellier-IZZI-MagIC.

Table 3
Triaxe Archeointensity Data

Test ID	Fragment	Specimen	T_1'-T_2 (°C)	H_{Lab} (μT)	NRM T_1' (%)	Slope R' (%)	F (μT)	F mean value per fragment ± σF (μT)
HZ-T01	HZ16Aa	HZ-T01a	275–520	50	81	5	39.9	39.6 ± 0.3
		HZ-T01b	265–520	40	81	6	39.3	
HZ-T02	HZ16Ab	HZ-T02a	180–520	50	80	1	42.5	43.5 ± 1.0
		HZ-T02b	220–520	45	78	0	44.4	
HZ-T03	HZ16Ac	HZ-T03a	200–520	45	93	−4	36.2	36.0 ± 0.2
		HZ-T03b	225–520	35	89	0	35.8	
HZ-T05	HZ16Ae	HZ-T05a	350–520	50	72	1	49.1	48.9 ± 0.3
		HZ-T05b	380–520	50	69	4	48.6	
HZ-T07	HZ16Ba	HZ-T07a	365–520	50	73	0	36.9	36.8 ± 0.2
		HZ-T07b	375–520	35	71	1	36.6	
HZ-T08	HZ16Bb	HZ-T08a	310–520	50	83	2	48.2	48.0 ± 0.2
		HZ-T08b	310–520	50	85	2	47.8	
HZ-T09	HZ16Bc	HZ-T09a	235–520	50	89	5	58.7	58.6 ± 0.2
		HZ-T09b	240–520	60	89	3	58.4	
HZ-T11	HZ16Bf	HZ-T11a	320–520	50	88	−1	41.4	41.6 ± 0.2
		HZ-T11b	335–520	40	89	−1	41.8	
HZ-T14	HZ16Cc	HZ-T14a	275–520	50	79	6	42.1	41.8 ± 0.3
		HZ-T14b	285–520	45	80	6	41.5	
HZ-T15	HZ16Cd	HZ-T15a	250–520	50	85	5	38.5	39.0 ± 0.5
		HZ-T15b	275–520	40	81	−1	39.5	
HZ-T17	HZ16Cf	HZ-T17a	295–520	50	73	6	39.5	39.5 ± 0.1
		HZ-T17b	280–520	40	75	5	39.4	
HZ-T19	HZ17Db	HZ-T19a	175–520	50	60	1	43.4	42.9 ± 0.5
		HZ-T19b	175–520	45	72	−2	42.4	
HZ-T22	HZ17Ea	HZ-T22a	245–520	50	77	5	41.0	40.6 ± 0.5
		HZ-T22b	260–520	40	76	3	40.1	
HZ-T23	HZ17Ee	HZ-T23a	275–520	50	89	4	38.1	37.9 ± 0.3
		HZ-T23b	275–520	40	90	2	37.6	
HZ-T24	HZ17Fa	HZ-T24a	305–520	50	81	5	41.0	41.1 ± 0.1
		HZ-T24b	305–520	40	81	5	41.1	
HZ-T25	HZ17Fe	HZ-T25a	175–520	50	79	−1	39.1	38.9 ± 0.3
		HZ-T25b	175–520	40	75	1	38.6	

We split a set of randomly selected Bronze Age pottery fragments from Tel Hazor (Table 3) into two groups. One group was sent to the IPGP laboratory without the archeological details of the fragments for Triaxe measurements and the other group was analyzed at the HUJI laboratory using the Thellier-IZZI-MagIC method. As the interpretation procedure of Thellier-IZZI-MagIC is fully automatic, the test is free of any subjective considerations for both methods. Sixteen fragments passed the Triaxe criteria (Table 3 and Figure 3), 15 fragments passed the Thellier-IZZI-MagIC criteria (Table 4), 4 fragments failed criteria in both methods, and 4 fragments failed criteria in one of the methods. Thirteen fragments that passed the selection criteria in both methods are shown in Figure 4. The agreement between the two datasets is excellent, displaying differences of less than 3 μT between the means of each fragment. When considering the error bounds, only two fragments show distinguishable values in the two methods, but their difference is smaller than 1 μT. We note that owing to the way the error bounds of the Thellier-IZZI-MagIC are calculated (see Section 2.2.1),

Table 4
Fragments Archeointensity From This Study

Fragment group	Fragment	*n* specimens	Method	STDEV-OPT mean (μT)	STDEV-OPT σ (μT)	Lower error bound (μT)	Higher error bound (μT)
Megiddo H-15	mgh15a	5	IZZI	59.9	0.5	56.7	63.2
	mgh15e	5	IZZI	52.9	0.1	51.5	55.9
	mgh15f	5	IZZI	49.2	0.8	42.2	52.8
	mgh15i	5	IZZI	54.5	0.1	49.9	56.9
	mgh15k	5	IZZI	58.3	0.1	54.9	63.2
Megiddo K-10	mgk10b	5	IZZI	56.0	0.1	52.9	58.5
	mgk10c	5	IZZI	54.6	0.2	50.4	58.6
	mgk10h	5	IZZI	47.3	0.8	43.1	51.8
	mgk10j	5	IZZI	47.1	1.6	43.7	52.2
	mgk10k	5	IZZI	44.8	0.3	42.5	48.0
Megiddo K-11	mgk11c	6	IZZI	51.8	3.0	47.4	56.3
	mgk11d	6	IZZI	57.6	1.5	55.3	60.4
	mgk11e	5	IZZI	46.6	0.1	44.6	49.9
	mgk11g	4	IZZI	53.0	0.1	44.5	54.8
Megiddo S-2	mgs2f	3	IZZI	36.6	0.1	34.0	37.4
	mgs2g	3	IZZI	39.8	0.1	36.2	41.9
Hazor XVI-A	HZ16Aa	7	IZZI + Triaxe	41.2	1.4	39.1	44.2
	HZ16Ab	6	IZZI + Triaxe	43.1	1.1	41.2	45.2
	HZ16Ac	5	IZZI + Triaxe	35.1	1.2	31.8	37.8
	HZ16Af	5	IZZI	39.1	1.3	35.2	41.7
Hazor XVI-B	HZ16Ba	5	IZZI + Triaxe	38.2	1.5	36.5	39.9
	HZ16Bc[a]	6	IZZI + Triaxe	57.9	0.6	53.2	60.6
	HZ16Bd	4	IZZI	38.0	0.9	36.2	40.5
	HZ16Be	5	IZZI	35.6	1.8	33.4	40.5
	HZ16Bf	6	IZZI + Triaxe	42.8	1.1	40.8	47.9
Hazor XVI-C	HZ16Ca	4	IZZI	34.8	0.5	30.1	38.5
	HZ16Cc	7	IZZI + Triaxe	42.2	0.5	40.4	43.8
	HZ16Cd	6	IZZI + Triaxe	38.6	0.7	37.3	40.7
	HZ16Cf	5	IZZI + Triaxe	38.1	1.4	35.2	39.5
Hazor XVII-D	HZ17Db	7	IZZI + Triaxe	42.7	0.4	41.9	43.5
	HZ17Dd	5	IZZI	39.6	1.0	37.2	42.2
	HZ17De	5	IZZI	38.0	0.1	35.7	39.7
Hazor XVII-E	HZ17Eb	4	IZZI	38.4	1.3	34.8	43.9
	HZ17Ed	5	IZZI	35.5	1.1	34.1	39.8
	HZ17Ee	6	IZZI + Triaxe	38.3	0.7	35.5	39.8
Hazor XVII-F	HZ17Fa	7	IZZI + Triaxe	39.8	1	38.1	41.5
	HZ17Fc	3	IZZI	38.9	2.6	35.4	42.2
	HZ17Fd	3	IZZI	43.4	3.4	43.4	46.8
	HZ17Fe	6	IZZI + Triaxe	38.9	0.3	36.0	39.4

[a]Outlier fragments.

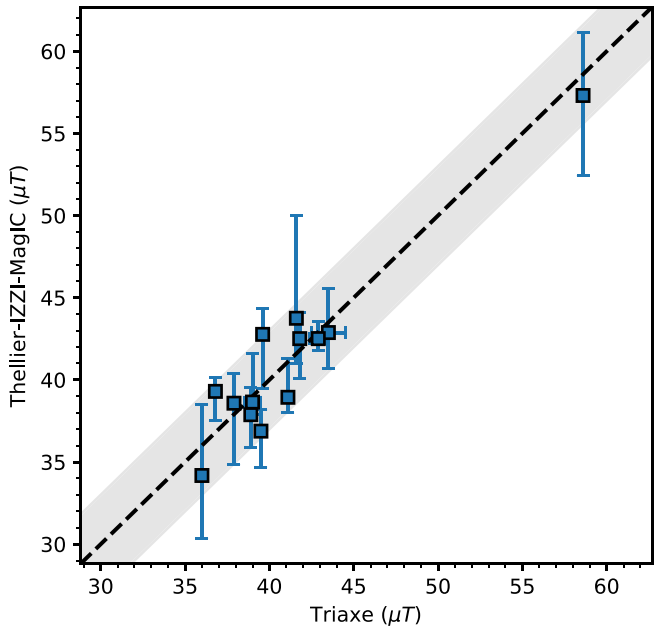

Figure 4. Comparison between fragments archeointensity obtained both using Thellier-IZZI-MagIC and Triaxe methods. The gray area shows ±3 μT envelope.

its error bars are larger. From this, we conclude that archeointensity data calculated using the two methods are indistinguishable.

3.2. Archeointensity Results

Out of 219 specimens, 181 passed the Thellier-IZZI-MagIC acceptance criteria, representing a success rate of 83%. Table S1 lists their statistics. Figure S3 displays histograms of the statistics used as selection criteria (Table 1), indicating the high quality of the accepted results. Histograms of the anisotropy and cooling rate correction factors are shown in Figure 5. The anisotropy correction of 27% of the specimens is higher than 10%, and the cooling rate correction of 10% of the specimens is higher than 10%. This emphasizes the importance of the two corrections. Also, it highlights the preference of fitting the cooling rate data to a line using three different cooling rates (e.g., Figure 2b), instead of the typical procedure of only two rates. All the raw measurement data and interpretations, including the ATRM, AARM, and cooling rate correction experiments, are available in the MagIC database (earthref.org/MagIC/16857).

Out of 52 fragments, 39 passed the Thellier-IZZI-MagIC criteria listed in Table 1, representing a success rate of 75%. We incorporated specimens analyzed using the Triaxe method in the fragment paleointensity calculation by assigning the value listed in Table 3 for each Triaxe specimen. The fragment results are presented in Table 4. Figure 6a shows fragment archeointensities plotted versus fragment group—level at Tel Megiddo and stratum/stage at Tel Hazor. Overall, there is a good agreement between fragments collected from the same group (archeological context) with some exceptions: one fragment from Megiddo H-15 had a lower value than the other four fragments; five fragments from Megiddo K-10 yielded two groups of results: two showing high values (~55 μT) and three indicating much lower values (near ~46 μT); one fragment from Hazor XVI-A showed a lower value than the other three fragments; one fragment from Hazor XVI-B showed significantly different values than the other four fragments from this stage. The latter fragment from Hazor XVI-B that showed values distinguishable from the rest of the fragments in the group, with error bounds distinct from all other fragments, is shown in red in Figure 6a, and is considered as an outlier. This fragment was not used in the calculation of the group mean. The scatter of the fragment data within the different groups can be explained by the nature of the potsherds found in the archeological context. Even after a careful preselection, the potsherds represent a time interval starting from the time a ceramic vessel was produced to the time it was deposited. Restricting ourselves to non-luxurious domestic vessels, this interval can last a few decades. Thus, by collecting several potsherds per context, we get a range of archeointensity values associated with the corresponding time interval. Also, we cannot eliminate the possibility of "contamination" of potsherds from other contexts, during the complex process of site formation. For example, the high outlier archeointensity value in Hazor XVI-B (~57 μT) can be explained

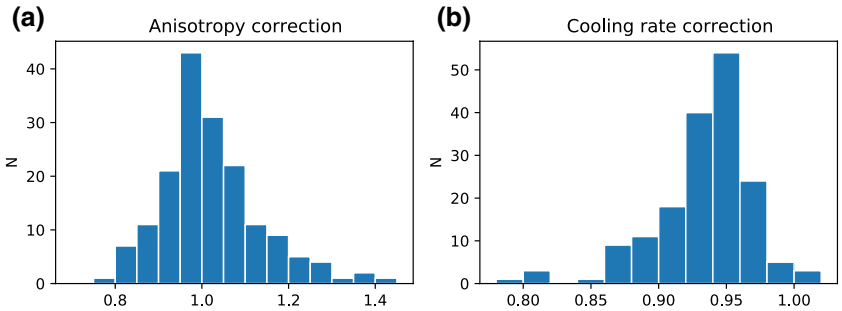

Figure 5. Histograms of the anisotropy and cooling rate correction values.

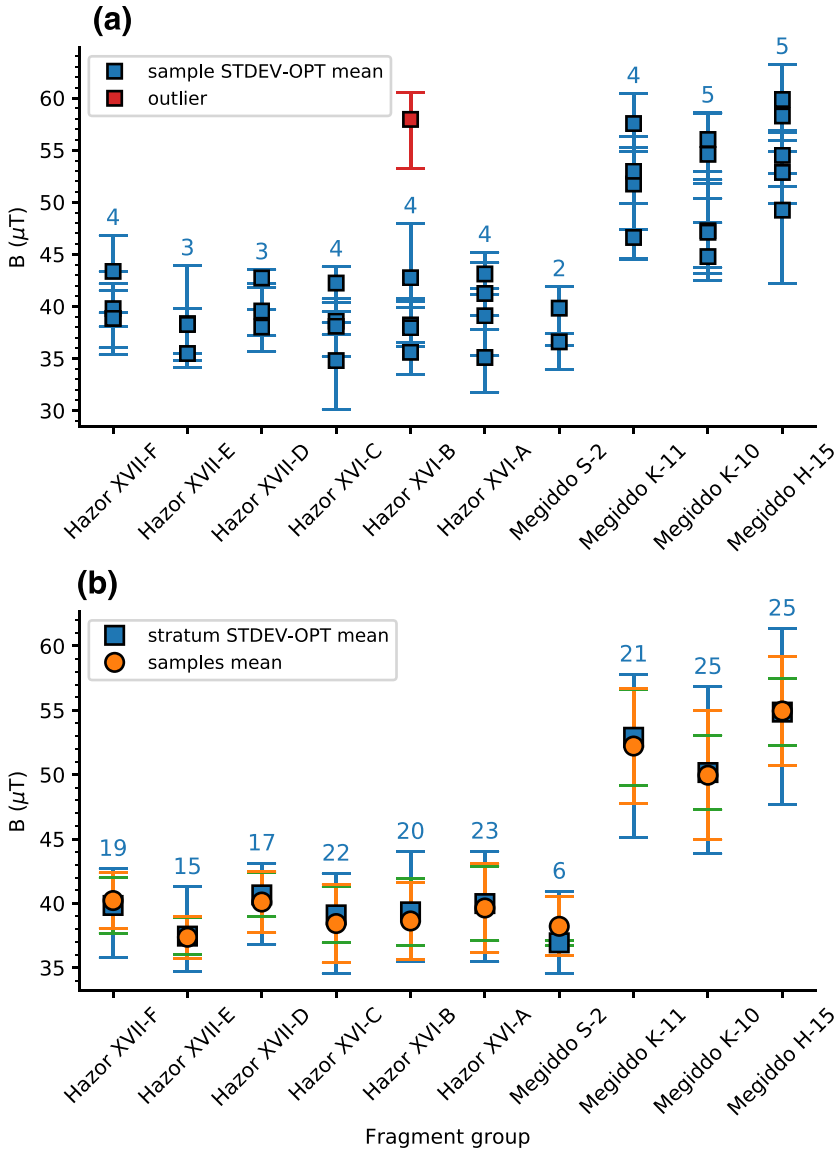

Figure 6. Archeointensity results. (a) Archeointensity data of pottery sherds (Table 4). The red symbol mark an outlier not used in group mean calculation. Numbers correspond to the number of fragments in each group excluding outliers. (b) Groups mean archeointensity values calculated by averaging fragments' means (orange circles and error bars) and by averaging specimens using the Thellier Auto Interpreter (blue squares, where green and blue error bars are the Thellier Auto Interpreter bounds and STDEV-OPT standard deviation, respectively). Numbers correspond to the number of specimens in each group.

by being younger in age, for example, from Hazor XV. For this reason, we took the approach of analyzing several fragments per group and tested the consistency within the fragment group before averaging them.

A mean value for each group (level, stratum, or stage), representing the time interval associated with the archeological context, was calculated using two approaches. The first is to average the mean values of the fragments (STDEV-OPT means in Table 4). This is the simplest and most straightforward approach. However, it does not take into account the different uncertainty of each fragment. The second approach is to use all the specimens from all the fragments passing the criteria (excluding the outlier fragment) and to calculate their STDEV-OPT mean and error bounds using the Thellier Auto Interpreter algorithm. The mean values calculated using these two approaches are shown in Figure 6b and listed in Table 5. The two calculation methods yield similar values of group means, but as expected, the error bounds calculated by the Thellier Auto Interpreter are larger.

Table 5
Group Archeointensity From Hazor and Megiddo, from this study and Shaar et al. (2016)

Fragment group	Radiocarbon age 68.2% probability interval (95.4% probability interval)[a]	Archeological age range (BCE)[b]	*N* Fragments	*n* specimens	Thellier auto interpreter				Mean of fragments	
					STDEV-OPT mean	STDEV-OPT σ	Lower bound	Upper bound	Mean	σ
Megiddo F-10	1545–1354 (1561–1313)	1550–1400	3	14	50.5	2.1	46.8	55.0	50.6	1.3
Megiddo H-15	1557–1509 (1572–1463)	1550–1475	5	25	54.9	2.6	47.7	61.4	54.9	4.3
Megiddo K-10	1581–1545 (1596–1535)	1600–1550	5	25	50.2	2.9	43.9	56.8	50	5.0
Megiddo K-11	1626–1579 (1643–1561)	1650–1600	4	21	52.9	3.7	45.1	57.8	52.2	4.5
Megiddo F-13		1900–1700	4	25	41.7	2.8	36.7	46.6	41.9	2.4
Megiddo S-2[c]	1942–1902 (1965–1886)	1950–1900	2	6	36.9	0.2	34.6	40.9	38.2	2.3
Hazor XV		1650–1450	3	9	49.6	0.5	47.6	53.7	49.9	0.5
Hazor XVI-A[d]		1800–1575 (1600)	4	23	40.0	2.9	35.5	44.0	39.6	3.4
Hazor XVI-B[d]		1800–1575 (1640)	4	20	39.3	2.6	35.5	44.0	38.6	3.0
Hazor XVI-C[d]		1800–1575 (1680)	4	22	39.1	2.2	34.6	42.3	38.4	3.0
Hazor XVII-D[d]		1800–1600 (1720)	3	17	40.7	1.7	36.8	43.1	40.1	2.4
Hazor XVII-E[d]		1800–1600 (1755)	3	15	37.5	1.4	34.7	41.3	37.4	1.6
Hazor XVII-F[d]		1800–1600 (1785)	4	19	39.8	2.1	35.8	42.7	40.2	2.1
Hazor XVIII[e]		2350–2200[e]	3	11	47.4	0.8	44.5	51.6	47.0	1.1

[a]Radiocarbon calculated using IntCal13 calibration curve following Martin et al. (2020). [b]Archeological ages for Megiddo reflect the age range of the context considering radiocarbon ages, historical constraints, material cultures and historical constraints; the above without radiocarbon ages for Hazor. [c]Destruction layer. [d]Age range based on archeomagnetic maximum ages calculated in Section 4.2 and historical constraints listed in Section 4.4. [e]Age range based on preliminary radiocarbon data (Lev et al., 2019).

4. Discussion

4.1. A Reduced Archeointensity Dataset

To clarify the sources for some of the noise displayed in the archeointensity compilation shown in Figure 1, we start by constructing a reduced archeointensity compilation assembled from contexts, which were dated using consistent archeological chronologies. We restrict ourselves to methods and selection criteria that were tested against each other: Triaxe (Gallet et al., 2006, 2008, 2014a; Gallet & Al-Maqdissi, 2010; Gallet & Le Goff, 2006), Thellier-Coe (Genevey et al., 2003), Thellier-IZZI-MagIC (Shaar et al., 2016), and Thellier-IZZI-MagIC + Triaxe (this study). Figure 7a shows data from Mari, Ebla, Megiddo, and Hazor. These are large stratified sites that include most of the data in the time span reported here, ca. 2300–1400 BCE. Table S2 outlines the archeological context of these data. It is important to note that data from Syrian sites were reported at both the fragment and the group levels, but they are plotted as group mean. Thus, each published data point in Figure 1 is an average of several fragments. The data from Megiddo and Hazor, however, were reported at the fragment level, thus each data point in Figure 1 is a specimen mean from a single fragment. To account for this difference and enable adequate comparison, we calculated a group mean for the previously published data from Megiddo and Hazor using the same Thellier Auto Interpreter technique deployed for the new data reported in the current study. These group means are listed in Table 5.

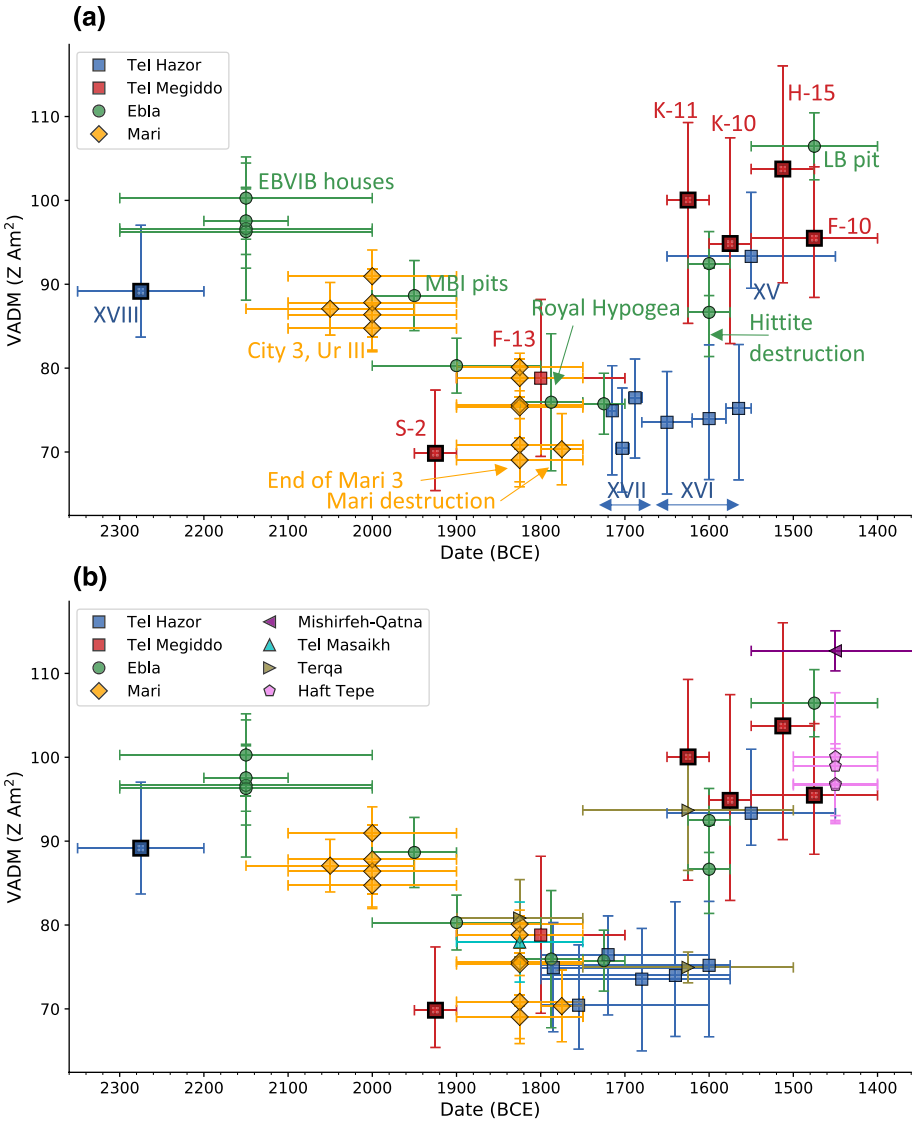

Figure 7. A reduced archeomagnetic compilation assembled following the criteria listed in Section 5.1. (a) Mari, Ebla, Hazor, and Megiddo, (b) same as (a) with additional data from nearby sites and adjustments of Hazor ages following the Bayesian analysis displayed in Figure 8 (Section 4.2).

The radiocarbon-dated contexts are highlighted with a bold frame in Figure 7a; they include Levels F-10, K-11, K-10, H-15, and S-2 at Megiddo and Stratum XVIII at Hazor. Stratum XVIII at Hazor has recently been dated to the interval between the second half of the 24th century and the 23rd century (Lev et al., 2019); since the analysis of this date is still in progress, we treat it merely as the best estimate. Figure 7b shows the same subset shown in Figure 7a with additional data from nearby sites – Mishirfeh-Qatna (Gallet & Al-Maqdissi, 2010), Tel Masaikh (Gallet et al., 2008), Terqa (Gallet et al., 2006, 2008), and Haft Tepe (Gallet et al., 2006) – obtained using the Triaxe or the Thellier-Coe methods.

Considering the error bounds both in age and archeointensity, the reduced dataset in Figures 7a and 7b shows agreement between the different data points except one significant discrepancy between Hazor XVI-A,B and the rest of the data in this time interval. This difference is explained by the different absolute chronologies adopted by the respective excavation teams. The archeological age range of Hazor XVII–XVI (MB II-III) was adjusted by the excavators to conform with the "Ultra Low Chronology", while the age of Ebla and Mari were adjusted to the "middle chronology" there (Figure S2). The debate in the archeological

literature regarding the absolute age of the Middle Bronze is long-standing and beyond the scope of this archeomagnetic article. Yet, in this case, the radiocarbon ages of the stratigraphic sequence at Megiddo Levels K-11, K-10, H-15, and F-10 provide objective chronological constraints to the archeological age of Hazor XVII–XVI: the high archeointensity data of Megiddo are significantly higher and different than Hazor XVII–XVI suggesting that the age limit of Hazor XVI-A should be shifted to earlier ages. The extent of this shift is calculated in Section 4.2 and its archeological implications are discussed in Section 4.4.

Megiddo Level S-2 (ca. 1950–1900 BCE) is a well-dated destruction layer that yielded the lowest archeointensity value in the whole interval, similar to the values of some of the data from Mari end of City 3. Only two fragments from Level S-2 pass our criteria because of severe secondary burning that resulted in secondary pTRM acquisition in most of the samples we analyzed. Yet, if confirmed with more fragments, this layer can constrain the duration of the low archeointensity episode that marks the minimum in the archeointensity curve. One option is that the minimum extended from the late 20th century to the late 17th century BCE. Another possibility is that there was a local maximum around 1800 BCE associated with Megiddo Level F-13 and the higher values in Mari. Graphically, the former interpretation would result in a "V-shaped" archeointensity curve, whereas the latter would make a "W-shaped" curve. We note that the low archeointensity values (virtual axis dipole moment [VADM] of 70–75 10^{12} Am^2) mark the lowest field during the past 4,500 years in the Levant and Mesopotamia.

4.2. Bayesian Modeling

To calculate an archeomagnetic age limit of the Middle Bronze levels at Hazor, we constructed a Bayesian archeointensity variation curve with 95% credible envelope using the reduced dataset displayed in Figure 7b. To minimize divergence of the Bayesian model due to edge effects, we expanded the modeled age interval and added data from the 25th to 24th centuries BCE and from the 14th to 13th centuries BCE (from Mari, Tell Gudeda, Chogha Zanbil, Tel Hazor, and Tel Megiddo (Gallet et al., 2006, 2008, 2020; Gallet & Butterlin, 2015; Gallet & Le Goff, 2006; Genevey et al., 2003; Shaar et al., 2016). For modeling purposes, we used the fragments' mean and standard deviation instead of the STDEV-OPT mean to keep consistency with the published data from the northern Levant and Mesopotamia. All ages of Hazor XVI–XVII were set to 1800–1550 BCE to account for all the possible age ranges within the Middle Bronze II/III (Figure S2) according to both the traditional chronology in the southern Levant and the middle chronology in Mesopotamia. The Bayesian curve was generated using the age hyperparameter reverse-jump Monte Carlo Markov Chain (AH-RJMCMC) algorithm, which is based on piecewise linear interpolations between randomly drawn vertices (Livermore et al., 2018) (https://github.com/plivermore/AH-RJMCMC1). Here we follow similar approach used in Gallet et al. (2020). The prior assumptions regarding the model and data are as follows: (i) the allowed range of vertices of VADM values is between 60 and 120 Z Am^2; (ii) the allowed number of vertices (K) is between $K_{min} = 1$ and $K_{max} = 150$; (iii) the archeological ages of the data are uniformly distributed (archeological age range in Table 5 and Table S2); (iv) normal distribution of the intensity data defined by the groups mean and standard deviation; (v) ages of stratified layers with overlapping age range must agree with the stratification order. The likelihood function is calculated for each data point at an age drawn from its age distribution by the difference between the intensity of the data to the intensity of the model, where the model is calculated from linear extrapolation between the vertices. The RJ-MCMC sampling algorithm represents a random walk through the space of models permitted by the likelihood function. Each perturbation of a model from its predecessor is done by shifting vertices in age and/or intensity and/or by adding or deleting a vertex. The perturbation is calculated using the following parameters: $\sigma_{move} = 30$ years, $\sigma_{change} = 10$ Z Am^2, and $\sigma_{birth} = 10$ Z Am^2 that describe the distributions of a vertex move in age, vertex change in intensity, and intensity of a new vertex born with respect to the extrapolated intensity at the vertex age. In our model, each perturbation includes one age resampling of the data in each perturbation (num_age_changes = 1). The chain length is 10^8. These parameters are close to the parameters defined by Gallet et al. (2020); for more details on the AH-RJMCMC code and algorithm, see Livermore et al. (2018).

Figure 8a displays the median and the 95% credible interval of the Bayesian model, showing that some portion of the prior age range of Hazor Middle Bronze falls outside the model 95% credible interval. Figures 8b and 8c show the joint posterior probability distribution of the age and the intensity (Livermore et al., 2018)

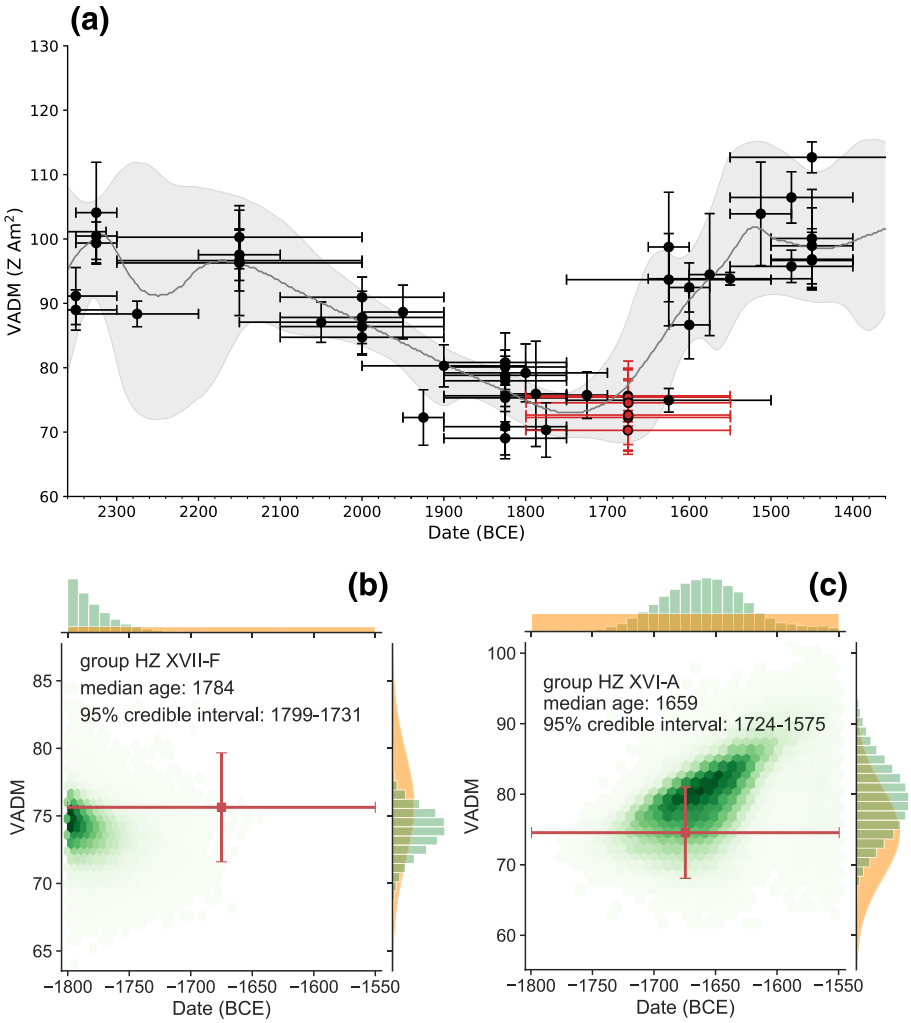

Figure 8. Archeomagnetic constraints of Hazor Middle Bronze strata using the method of Livermore et al. (2018). (a) Bayesian 95% confidence interval, with prior ages of Hazor Middle Bronze shown in red. Errorbars show groups mean and standard deviation. (b and c) Joint posterior probability distribution of the age and the intensity of fragment groups HZ VII-F and HZ VI-A. The priors are shown in orange and the posteriors are shown in green.

of fragment groups Hazor XVI-A and Hazor XVII-F. The 95% credible bounds suggest that Hazor XVII-F started in the beginning of the 18th century and that Hazor XVI-A ended before ca. 1575 BCE. With these archeomagnetic constraints in hand, we reassign the age range of Hazor XVII–XVI between 1800 BCE (the beginning of Middle Bronze II according to the middle chronology) and 1575 BCE (new archeomagnetic constraints) keeping as much as possible the original internal division within the strata provided by the excavators. We assign wide error age bounds to fit the historical constraints on one hand (see Section 4.4) and the archeomagnetic constraints on the other hand. The archeomagentcally revised ages of Hazor XVII–XVI are listed in Table 5 and shown in Figure 7b. The Bayesian archeointensity variation curve with 95% credible envelope are given in Table S3.

4.3. Comparison With Nearby Data

In Figure 7a, we synchronized the datasets of Mari, Ebla, Hazor, and Megiddo, because these sites are the source for the majority of the data in Figure 1; each of these sites includes a detailed succession of strata dated in a consistent manner; data were analyzed by archeointensity methods that were cross-tested with each other; and six radiocarbon-dated contexts enable partly tying the data to absolute ages. Data from other

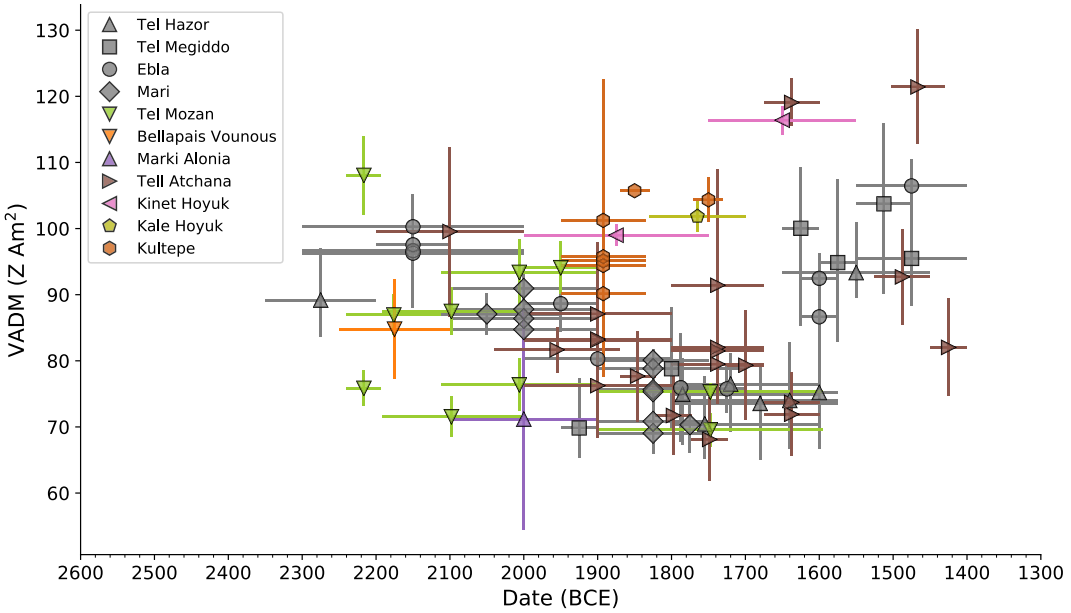

Figure 9. Comparison of the reduced synchronized archeomagnetic compilation (Figure 8b, gray symbols) and other published data from nearby sites.

nearby sites, which were analyzed using similar archeomagnetic methods and dated following the middle chronology are shown in Figure 7b and are in agreement with the rest of the data. Both datasets displayed in Figures 7a and 7b were used to construct the Bayesian model. Figure 9 shows the rest of the data, which were obtained using methods that were not tested against Thellier-IZZI-MagIC or Triaxe. Tell Mozan (Stillinger et al., 2015) was analyzed using the Thellier-IZZI protocol with anisotropy and cooling rate corrections, but with different acceptance criteria than Thellier-IZZI-MagIC. Data are reported at the fragment level, typically with 1–2 fragments per age group, with some apparent internal inconsistency among fragments from the same age. The one group that includes at least two fragments with the same archeointensity value is dated between 1900 and 1600 BCE. The low value of this group is in agreement with the archeointensity minimum in the synchronized compilation. Two pottery fragment groups from Cyprus—Bellapais Vounous and Marki Alonia (Ertepinar et al., 2020)—analyzed using the microwave method—are in agreement with the synchronized dataset considering their error bars, but are not perfectly aligned with it.

The radiocarbon-dated data from Turkey can potentially provide critical key chronological tie points to the archeoinensity compilation. Some of the data from Tell Atchana and Kinet Hoyuk (Ertepinar et al., 2020) and Kale Höyük and Kültepe (Ertepinar et al., 2016) are in agreement with the synchronized dataset, but other data show significantly different values. These data were analyzed using the microwave method and/or the Coe or the IZZI variants of the Thellier method and/or the multispecimen method. We note that the acceptance criteria used in these datasets are significantly weaker than the criteria used in the Thellier-IZZI-MagIC used here (Table 1). For example, most of the Anatolian data use fraction parameter (*f*-statistic of Coe et al. [1978]) ≥0.35, whereas in the reduced compilation, we use fraction parameter (FRAC, Table 1) ≥0.79. As the raw measurement were not published, we could not reprocess these data using the same interpretation algorithm, selection criteria, and averaging schemes as in this study.

Figures 9 and 1 demonstrate that, when attempting to construct a coherent regional archeointensity compilation from the entire published data by a simple stack of modern data, there is a considerable noise that masks the true trend of the geomagnetic field behavior. We repeat that the sources of the noise are uncertainties in the archeological age determinations as well as from difference in the paleointensity interpretation approaches. Therefore, unless each of the discrepancies in Figure 9 are rigorously assessed, we suggest that future geomagnetic models that include the time interval 2300–1400 BCE use the synchronized compilation in Figure 7b (Table 5 and Table S2).

4.4. Implications to Archeological Chronologies of the Middle Bronze

Our results for Strata XVII–XVI at Hazor and Level K-11 at Megiddo touch on two parallel, but related debates regarding the chronology of the first half of the second millennium BCE in the Ancient Near East. The first is the dispute over the historical Mesopotamian chronology, which involves vast and complex textual and archeological data. The focus of the discussion is the dating of the first dynasty in Babylon and its well-known king, Hammurabi. At least five chronological systems, stemming from astronomical observations of Venus in the eighth year of the 10th ruler of the dynasty, Ammisaduqa, have been proposed (Cryer, 1995; Rochberg-Halton, 1988; Schwartz, 2008). The Middle Chronology (which dates Hamurrabi's reign to 1792–1750 BCE, and the destruction of Mari to 1760 BCE) is favored in recent years (see summary in Ben-Tor [2004] and Manning et al. [2016]). The second debate involves the chronology of the Middle Bronze in the southern Levant; for the current article, the key question is the transition from the Middle Bronze I to the Middle Bronze II (Figure S2). At least three systems—high, traditional, and low—are discussed. In an attempt to resolve these disputes, scholars have recently turned to radiocarbon studies (e.g., Manning et al. [2016] for Mesopotamian chronology; Bietak [2013]; Höflmayer [2017]; Höflmayer et al. [2016]; Kutschera et al. [2012] for the southern Levant).

Hazor is involved in the Mesopotamian chronology debate "by proxy" through its link to the Mari tablets (see summary in Ben-Tor [2004]). According to the Middle Chronology, Mari was destroyed by Hammurabi in 1760 BCE; according to the Ultra Low Chronology, it was devastated in 1664 BCE. Hazor is mentioned in the Mari texts, which belong to the last phase of its history, before its destruction by Hammurabi (Malamat, 1992), and Mari is mentioned in a tablet found at Hazor (Horowitz & Wasserman, 2000); the suggestion that Hazor of the Mari texts is not the site discussed here (Astour, 1991) has been dismissed (Ben-Tor, 2004). The excavators of Hazor argued that the Hazor mentioned in the Mari texts must be the prosperous city which covered both the upper and lower parts of the mound—the largest site in Canaan in the Middle Bronze Age (Ben-Tor, 2004; Yadin, 1972). This description fits the advanced stage of Hazor XVII and/or the early stage of Hazor XVI (the latter continued into the Middle Bronze III, meaning that it outlived Mari [Ben-Tor & Bechar, 2017; Ben-Tor et al., 2017]).

Hazor XVII–XVI as well as the destruction of Mari is not radiocarbon dated, but Megiddo can serve here as a chronological anchor and proxy. Our magnetic intensity data show that Hazor strata XVII–XVI are earlier than Megiddo K-11 (Figures 7 and 8), the duration of which is radiocarbon dated to 1626–1579 BCE (68.2% probability range). The pottery assemblages of Hazor strata XVII–XVI cover the Middle Bronze II and the Middle Bronze III. Megiddo K-11 could have started in the late Middle Bronze II and continued into the early days of the Middle Bronze III. Middle Bronze II Megiddo K-12 was probably contemporaneous with the early days of Hazor XVI and, possibly, the late days of XVII (perhaps also Level K-13, but thorough work on the ceramic assemblages of both Levels K-12 and K-13 has not yet been carried out). The missing datum in order to wrap up all this information is the earliest possible date for "Greater Hazor," sometime during the life of Stratum XVII. Fixing it depends on the date of transition from the Middle Bronze I to the Middle Bronze II (ceramic phases), which is also debated, between ca. 1850 and close to 1700 BCE (see summary in Höflmayer [2017], Figure S2). Finally, we should note that judging from its material culture, including the six phases of construction (Ben-Tor et al., 2017), "Greater Hazor" must be given a long-enough duration.

From the perspective of Hazor and Mari, when put together, all these can be summarized as follows (emphasis only on Middle and Ultra Low Mesopotamian chronology):

- Assuming the destruction of Mari at 1664 BCE (Ultra Low Chronology), MB II as the ceramic phase of Hazor advanced XVII and early XVI, and the traditional chronology for the Middle Bronze I/II transition in the southern Levant (ca. 1750 BCE), then the overlap between Hazor and Mari can be placed at 1750–1664 BCE
- Assuming the above, with the southern Levantine low chronology replacing the traditional chronology for the Middle Bronze I/II transition in the southern Levant (ca. 1710–1700 BCE), then the overlap between Hazor and Mari can be placed at ca. 1710/1700–1664 BCE – a sufficient period of time, considering that Greater Hazor outlived Mari

- Assuming the destruction of Mari in 1760 BCE (Middle Chronology) does not work with the traditional Middle Bronze chronology in the southern Levant, which puts the Middle Bronze I/II transition ca. 1750 BCE; evidently, in this case, Hazor prospers after Mari is destroyed. It is possible, though, if one turns to the southern Levantine high chronology for the Middle Bronze I/II transition at ca. 1850/1800 (Höflmayer, 2017). In this case, the Hazor-Mari overlap would fall at ca. 1850/1800–1760 BCE

In the compilation in Figure 7, we still cannot resolve the chronological debates concerning the absolute chronology of the destruction of Mari and the Middle Bronze I/II transition in the southern Levant. Instead, we plot the archeointensity data from Mari as published (Gallet et al., 2006; Gallet et al., 2008; Gallet & Le Goff, 2006; Genevey et al., 2003), assuming its destruction in 1760 BCE (Middle Chronology) and Hazor XVI–XVII between 1800 and 1750 BCE as calculated from the archeomagnetic Bayesian model.

5. Conclusions

A considerable amount of archaointensity data were published from the northern Levant and Mesopotamia for the time interval between the 23rd and the 15th centuries BCE. Yet, a simple stack of the data displays large inconsistencies that cannot be easily resolved, due to the application of different archeointensity methods and selection criteria, as well as different historical-archeological chronological schemes. Here we established a basis for comparison between data derived by the Thellier-IZZI-MagIC and the Triaxe methods from a blind test that resulted in indistinguishable results or a difference that was less than 1 μT. Based on the conclusion that the two methods are compatible, we constructed a reduced and synchronized archeointensity compilation using 37 fragment groups from Mari, Ebla, Hazor, and Megiddo, which includes new data from 10 groups from Hazor and Megiddo. Additional eight fragment groups from four other nearby sites are in agreement with the reduced compilation and hence we include them in our compilation. The reduced compilation is constrained by five radiocarbon-dated levels at Megiddo and one radiocarbon-dated stratum at Hazor. The compilation illustrates a prominent field intensity minimum centered around the 18th century BCE, which spans over at least 200 years and marks the lowest field intensity in the Levant in the past 4,500 years.

A comparison of the synchronized-reduced compilation with other data, derived using different archeointensity methods and/or different acceptance criteria, is more complicated. Discrepancies can be attributed to archeointensity biases, different archeological chronologies and age terminologies, or problems of archeological contexts. As these biases can be problematic to address without rigorous comparison between the methods, we suggest using the reduced compilation presented here (Table 5 and Table S2) for modeling purposes and archeomagnetic dating rather than using the entire set of published data.

From the perspective of archeological chronology, the new data may provide a new tool for assessing the chronology of the first half of the second millennium BCE in Mesopotamia and the northern Levant, and the chronology of the Middle Bronze phases in the southern Levant. In particular, the new archeointensity data provide constraints to the age of the Middle Bronze II/III strata at Tel Hazor.

Acknowledgments
We would like to thank Amnon Ben-Tor, the director of the excavations at Hazor, for his assistance and guidance. Yves Gallet thanks Maxime Le Goff, Phil Livermore, and Alexandre Fournier for very helpful discussions. The study was supported by the Israel Science Foundation (ISF) (grant 1364/15). This project has received funding from the European Research Council (ERC) under the European Union's Horizon 2020 research and innovation programme (grant agreement No 804490). This study was partly financed by INSU-CNRS program PNP. This is IPGP contribution no. 4174. Work on the Megiddo samples was supported by the Dan David Foundation and grants from Mark Weissman and Jacques Chahine. We thank Lisa Tauxe and an anonymous reviewer for their review.

Data Availability Statement

The Thellier-IZZI-MagIC paleointensity measurements data are available in the MagIC database (earthref.org/MagIC/16857).

References

Aitken, M. J., Allsop, A. L., Bussell, G. D., & Winter, M. B. (1984). Geomagnetic intensity in Egypt and Western Asia during the 2nd Millennium BC. *Nature*, *310*(5975), 305–306.

Arneitz, P., Egli, R., Leonhardt, R., & Fabian, K. (2019). A Bayesian iterative geomagnetic model with universal data input: Self-consistent spherical harmonic evolution for the geomagnetic field over the last 4000 years. *Physics of the Earth and Planetary Interiors*, *290*, 57–75.

Astour, M. C. (1991). The location of Hasura of the Mari texts. *Maarav*, *7*, 51–65.

Athavale, R. N. (1969). Intensity of geomagnetic field in Prehistoric Egypt. *Earth and Planetary Science Letters*, *6*(3), 221–224.

Ben-Tor, A. (2004). Hazor and chronology. *Egypt and the Levant*, *14*, 45–67.
Ben-Tor, A. (2015). *Hazor: Canaanite Metropolis, Israelite City*. Jerusalem: Biblical Archaeology Society and Israel exploration Society.
Ben-Tor, A., & Bechar, S. (2017). Introduction. In A. Ben-Tor, S. Zuckerman, S. Bechar, & D. Sandhaus (Eds.), *Hazor VII – The 1990-2012 excavations – The Bronze Age* (pp. 1–3). Jerusalem: Israel Exploration Society.
Ben-Tor, A., Zuckerman, S., Bechar, S., & Weinblatt, D. (2017). The Middle Bronze Age. In A. Ben-Tor, S. Zuckerman, S. Bechar, & D. Sandhaus (Eds.), *Hazor VII – The 1990-2012 excavations: The Bronze Age* (pp. 20–65). Jerusalem: Israel Exploration Society.
Ben-Yosef, E., Millman, M., Shaar, R., Tauxe, L., & Lipschits, O. (2017). Six centuries of geomagnetic intensity variations recorded by royal Judean stamped jar handles. *Proceedings of the National Academy of Sciences of the United States of America*, *114*(9), 2160–2165.
Ben-Yosef, E., Ron, H., Tauxe, L., Agnon, A., Genevey, A., Levy, T. E., et al. (2008). Application of copper slag in geomagnetic archaeointensity research. *Journal of Geophysical Research: Solid Earth*, *113*(B8). http://doi.org/10.1029/2007jb005235
Ben-Yosef, E., Tauxe, L., Levy, T. E., Shaar, R., Ron, H., & Najjar, M. (2009). Geomagnetic intensity spike recorded in high resolution slag deposit in Southern Jordan. *Earth and Planetary Science Letters*, *287*(3–4), 529–539.
Bietak, M. (2013). Antagonisms in historical and radiocarbon chronology. In A. Shortland C. Ramsey M. Dee, & F. Brock (Eds.), *Radiocarbon and the chronologies of Ancient Egypt* (pp. 76–109). Oxford, UK: Oxbow Books.
Campuzano, S. A., Gomez-Paccard, M., Pavon-Carrasco, F. J., & Osete, M. L. (2019). Emergence and evolution of the South Atlantic anomaly revealed by the new paleomagnetic reconstruction SHAWQ2k. *Earth and Planetary Science Letters*, *512*, 17–26.
Coe, R. S. (1967). Paleo-intensities of Earth's magnetic field determined from Tertiary and Quaternary rocks. *Journal of Geophysical Research*, *72*(12), 3247–3262.
Coe, R. S., Gromme, S., & Mankinen, E. (1978). Geomagnetic paleointensities from radiocarbon-dated lava flows on Hawaii and question of Pacific nondipole low. *Journal of Geophysical Research*, *83*(B4), 1740–1756.
Cryer, F. H. (1995). Chronology: Issues and problems. In J. M. Sasson, J. Baines, G. M. Beckman, & K. S. Rubinson (Eds.), *Civilizations of the Ancient Near East* (pp. 651–664). New York, NY: Macmillan.
Davies, C., & Constable, C. (2017). Geomagnetic spikes on the core-mantle boundary. *Nature Communications*, *8*(1), 1–11.
Ertepinar, P., Hammond, M. L., Hill, M. J., Biggin, A. J., Langereis, C. G., Herries, A. I. R., et al. (2020). Extreme geomagnetic field variability indicated by Eastern Mediterranean full-vector archaeomagnetic records. *Earth and Planetary Science Letters*, *531*, 1–16. http://doi.org/10.1016/j.epsl.2019.115979
Ertepinar, P., Langereis, C. G., Biggin, A. J., de Groot, L. V., Kulakoglu, F., Omura, S., & Suel, A. (2016). Full vector archaeomagnetic records from Anatolia between 2400 and 1350 BCE: Implications for geomagnetic field models and the dating of fires in antiquity. *Earth and Planetary Science Letters*, *434*, 171–186.
Ertepinar, P., Langereis, C. G., Biggin, A. J., Frangipane, M., Matney, T., Okse, T., & Engin, A. (2012). Archaeomagnetic study of five mounds from Upper Mesopotamia between 2500 and 700 BCE: Further evidence for an extremely strong geomagnetic field ca. 3000 years ago. *Earth and Planetary Science Letters*, *357*, 84–98.
Fox, J. M. W., & Aitken, M. J. (1980). Cooling-rate dependence of thermoremanent magnetization. *Nature*, *283*(5746), 462–463.
Gallet, Y., & Al-Maqdissi, M. (2010). Archeomagnetism in Mishirfeh-Qatna: New data on the evolution of intensity in the earthly magnetic field in the Middle East during the last millenia. *Akkadica*, *131*(1), 29–46.
Gallet, Y., & Butterlin, P. (2015). Archeological and geomagnetic implications of new archeomagnetic intensity data from the early Bronze high terrace "Massif Rouge' at Mari (Tell Hariri, Syria). *Archaeometry*, *57*, 263–276.
Gallet, Y., D'Andrea, M., Genevey, A., Pinnock, F., Le Goff, M., & Matthiae, P. (2014a). Archeomagnetism at Ebla (Tell Mardikh, Syria). New data on geomagnetic field intensity variations in the Near East during the Bronze Age. *Journal of Archaeological Science*, *42*, 295–304.
Gallet, Y., Fortin, M., Fournier, A., Le Goff, M., & Livermore, P. (2020). Analysis of geomagnetic field intensity variations in Mesopotamia during the third millennium BC with archeological implications. *Earth and Planetary Science Letters*, *537*, 1–13.
Gallet, Y., Genevey, A., Le Goff, M., Fluteau, F., & Ali Eshraghi, S. (2006). Possible impact of the Earth's magnetic field on the history of ancient civilizations. *Earth and Planetary Science Letters*, *246*(1–2), 17–26.
Gallet, Y., Genevey, A., Margueron, J. C., Le Goff, M., Thébault, E., Matthiae, P., et al. (2014b). Exemples de chronologie archéomagnétique à Mari/Tell Hariri inInstitut Français du Proche-Orient Beyrouth. In P. Butterlin, J. C. Margueron, & B. Muller (Eds.), *Syria Supplement 2* (pp. 217–230). Beirut, Lebanon: Institut français du Proche-Orient.
Gallet, Y., & Le Goff, M. (2006). High-temperature archeointensity measurements from Mesopotamia. *Earth and Planetary Science Letters*, *241*(1–2), 159–173.
Gallet, Y., Le Goff, M., Genevey, A., Margueron, J., & Matthiae, P. (2008). Geomagnetic field intensity behavior in the Middle East between similar to 3000 BC and similar to 1500 BC. *Geophysical Research Letters*, *35*(12). https://doi.org/10.1029/2007gl031991
Gallet, Y., Montana, M. M., Genevey, A., Garcia, X. C., Thebault, E., Bach, A. G., et al. (2015). New Late Neolithic (c. 7000-5000 BC) archeointensity data from Syria. Reconstructing 9000 years of archeomagnetic field intensity variations in the Middle East. *Physics of the Earth and Planetary Interiors*, *238*, 89–103.
Games, K. P. (1980). The magnitude of the archeomagnetic field in Egypt between 3000 and 0 BC. *Geophysical Journal International*, *63*(1), 45–56.
Genevey, A., & Gallet, Y. (2002). Intensity of the geomagnetic field in western Europe over the past 2000 years: New data from ancient French pottery. *Journal of Geophysical Research*, *107*(B11). https://doi.org/10.1029/2001JB000701
Genevey, A. S., Gallet, Y., & Margueron, J. C. (2003). Eight thousand years of geomagnetic field intensity variations in the eastern Mediterranean. *Journal of Geophysical Research-Solid Earth*, *108*(B5). https://doi.org/10.1029/2001jb001612
Genevey, A., Gallet, Y., Rosen, J., & Le Goff, M. (2009). Evidence for rapid geomagnetic field intensity variations in Western Europe over the past 800 years from new French archeointensity data. *Earth and Planetary Science Letters*, *284*(1–2), 132–143.
Halgedahl, S. L., Day, R., & Fuller, M. (1980). The effect of cooling rate on the intensity of weak-field trm in single-domain magnetite. *Journal of Geophysical Research*, *85*(NB7), 3690–3698.
Hartmann, G. A., Genevey, A., Gallet, Y., Trindade, R. I. F., Etchevarne, C., Le Goff, M., & Afonso, M. C. (2010). Archeointensity in Northeast Brazil over the past five centuries. *Earth and Planetary Science Letters*, *296*(3–4), 340–352.
Hartmann, G. A., Genevey, A., Gallet, Y., Trindade, R. I. F., Le Goff, M., Najjar, R., et al. (2011). New historical archeointensity data from Brazil: Evidence for a large regional non-dipole field contribution over the past few centuries. *Earth and Planetary Science Letters*, *306*(1–2), 66–76.
Hellio, G., & Gillet, N. (2018). Time-correlation-based regression of the geomagnetic field from archeological and sediment records. *Geophysical Journal International*, *214*(3), 1585–1607.
Hervé, G., Faβbinder, J., Gilder, S. A., Metzner-Nebelsick, C., Gallet, Y., Genevey, A., et al. (2017). Fast geomagnetic field intensity variations between 1400 and 400 BCE: New archaeointensity data from Germany. *Physics of the Earth and Planetary Interiors*, *270*, 143–156. https://doi.org/10.1016/j.pepi.2017.07.002

Hervé, G., & Lanos, P. (2018). Improvements in archeomagnetic dating in Western Europe from the late Bronze to the late Iron Ages: An alternative to the problem of the Hallstattian radiocarbon plateau. *Archaeometry*, *60*(4), 870–883.
Hext, G. R. (1963). The estimation of second-order tensors, with related tests and designs. *Biometrika*, *50*, 353–357.
Höflmayer, F. (2017). A radiocarbon chronology for the Middle Bronze Age southern levant. *Journal of Ancient Egyptian Interconnections*, *13*(1), 20–33.
Höflmayer, F., Kamlah, L., Sader, H., Dee, M. W., Kutschera, W., Wild, E. M., & Riehl, S. (2016). New evidence for Middle Bronze Age chronology and synchronisms in the Levant: Radiocarbon dates from Tell el-Burak, Tell el-Dab'a, and Tel Ifshar compared. *Bulletin of the American Schools of Oriental Research*, *375*(1), 53–76.
Horowitz, W., & Wasserman, N. (2000). An old Babylonian letter from Hazor with mention of Mari and Ekallātum. *Israel Exploration Journal*, *50*, 169–174.
Hussain, A. G. (1983). Archaeomagnetic investigations in Egypt – Inclination and field intensity determinations. *Journal of Geophysics*, *53*(3), 131–140.
Kirschvink, J. (1980). The least-squares line and plane and the analysis of paleomagnetic data. *Geophysical Journal of the Royal Astronomical Society*, *62*(3), 699–718.
Korte, M., Constable, C., Donadini, F., & Holme, R. (2011). Reconstructing the Holocene geomagnetic field. *Earth and Planetary Science Letters*, *312*(3–4), 497–505.
Kutschera, W., Bietak, M., Wild, E. M., Ramsey, C. B., Dee, M., Golser, R., et al. (2012). The chronology of Tell el-Daba: A crucial meeting point of C-14 dating, Archeology, and Egyptology in the 2nd millennium BC. *Radiocarbon*, *54*(3-4), 407–422. https://doi.org/10.1017/s0033822200047172
Le Goff, M., & Gallet, Y. (2004). A new three-axis vibrating sample magnetometer for continuous high-temperature magnetization measurements: Applications to paleo- and archeo-intensity determinations. *Earth and Planetary Science Letters*, *229*(1–2), 31–43.
Lev, R., Bechar, S., & Boaretto, E. (2019). Radiocarbon absolute chronology of EBIII–Intermediate Bronze Age–Middle Bronze Age sequence at Tel Hazor, and its synchronization with the Northern Levant. *2019 ASOR Annual Meeting*.
Livermore, P. W., Fournier, A., & Gallet, Y. (2014). Core-flow constraints on extreme archeomagnetic intensity changes. *Earth and Planetary Science Letters*, *387*, 145–156.
Livermore, P. W., Fournier, A., Gallet, Y., & Bodin, T. (2018). Transdimensional inference of archeomagnetic intensity change. *Geophysical Journal International*, *215*(3), 2008–2034.
Malamat, A. (1992). Mari and Hazor: The implication for the Middle Bronze age chronology. *Ägypten und Levante/Egypt and the Levant*, *3*, 121–123.
Manning, S. W., Griggs, C. B., Lorentzen, B., Barjamovic, G., Ramsey, C. B., Kromer, B., & Wild, E. M. (2016). Integrated tree-ring-radiocarbon high-resolution timeframe to resolve earlier second Millennium BCE Mesopotamian chronology. *PloS One*, *11*(7).
Martin, M. A. S., Finkelstein, I., & Piasetzky, E. (2020). Radiocarbon-dating the late Bronze Age: Cultural and historical considerations on Megiddo and beyond. *Bulletin of the American Schools of Oriental Research*, *384*, 211–240.
Nagata, T., Arai, Y., & Momose, K. (1963). Secular variation of the geomagnetic total force during the last 5000 years. *Journal of Geophysical Research*, *68*(18), 5277–5282.
Nilsson, A., Holme, R., Korte, M., Suttie, N., & Hill, M. (2014). Reconstructing Holocene geomagnetic field variation: New methods, models and implications. *Geophysical Journal International*, *198*(1), 229–248.
Odah, H. (1999). Improvement of the secular variation curve of the geomagnetic field in Egypt during the last 6000 years. *Earth Planets and Space*, *51*(12), 1325–1329.
Odah, H. (2004). Geomagnetic intensity in upper Egypt between 2900 BC and 800 AD. *Journal of Applied Geophysics*, *3*(2), 205–212.
Odah, H., Heider, F., Hussain, A. G., Hoffmann, V., Soffel, H., & Elgamili, M. (1995). Paleointensity of the geomagnetic-field in Egypt from 4000 BC to 150 AD using the Thellier method. *Journal of Geomagnetism and Geoelectricity*, *47*(1), 41–58.
Osete, M. L., Molina-Cardín, A., Campuzano, S. A., Aguilella-Arzo, G., Barrachina-Ibañez, A., Falomir-Granell, F., et al. (2020). Two archaeomagnetic intensity maxima and rapid directional variation rates during the Early Iron Age observed at Iberian coordinates. Implications on the evolution of the Levantine Iron Age Anomaly. *Earth and Planetary Science Letters*, *533*, 116047. http://doi.org/10.1016/j.epsl.2019.116047
Paterson, G. A., Tauxe, L., Biggin, A. J., Shaar, R., & Jonestrask, L. C. (2014). On improving the selection of Thellier-type paleointensity data. *Geochemistry, Geophysics, Geosystems*, *15*(4), 1180–1192. https://doi.org/10.1002/2013gc005135
Pavón-Carrasco, F. J., Osete, M. L., Torta, J. M., & De Santis, A. (2014). A geomagnetic field model for the Holocene based on archaeomagnetic and lava flow data. *Earth and Planetary Science Letters*, *388*, 98–109.
Peters, I., Tauxe, L., & Ben-Yosef, E. (2018). Archaeomagnetic dating of pyrotechnological contexts: A case study for copper smelting sites in the Central Timna Valley, Israel. *Archaeometry*, *60*(3), 554–570.
Regev, J., Finkelstein, I., Adams, M. J., & Boaretto, E. (2014). Wiggled-matched 14C chronology of early Bronze Megiddo and the synchronization of Egyptian and Levantine chronologies. *Egypt and the Levant*, *24*, 241–264.
Rochberg-Halton, F. (1988). *Aspects of Babylonian celestial divination: The lunar eclipse tablets of Enuma Anu Enlil*. Vienna: Berger & Söhne.
Rogers, J., Fox, J. M. W., & Aitken, M. J. (1979). Magnetic-anisotropy in ancient pottery. *Nature*, *277*(5698), 644–646.
Schwartz, G. M. (2008). Problems of chronology: Mesopotamia, Anatolia and the Syro-Levantine region. In J. Aruz, K. Benzel, & J. M. Evans (Eds.), *Beyond Babylon: Art, trade and diplomacy in the second millennium B.C.* (pp. 450–452). New York, NY: Metropolitan Museum of Art.
Selkin, P. A., & Tauxe, L. (2000). Long-term variations in palaeointensity. *Philosophical Transactions of the Royal Society of London Series a-Mathematical Physical and Engineering Sciences*, *358*(1768), 1065–1088.
Shaar, R., Ben-Yosef, E., Ron, H., Tauxe, L., Agnon, A., & Kessel, R. (2011). Geomagnetic field intensity: How high can it get? How fast can it change? Constraints from Iron Age copper slag. *Earth and Planetary Science Letters*, *301*(1–2), 297–306.
Shaar, R., & Tauxe, L. (2013). Thellier GUI: An integrated tool for analyzing paleointensity data from Thellier-type experiments. *Geochemistry, Geophysics, Geosystems*, *14*(3), 677–692. https://doi.org/10.1002/ggge.20062
Shaar, R., Tauxe, L., Ben-Yosef, E., Kassianidou, V., Lorentzen, B., Feinberg, J. M., & Levy, T. E. (2015). Decadal-scale variations in geomagnetic field intensity from ancient Cypriot slag mounds. *Geochemistry, Geophysics, Geosystems*, *16*(1), 195–214. https://doi.org/10.1002/2014gc005455
Shaar, R., Tauxe, L., Ron, H., Ebert, Y., Zuckerman, S., Finkelstein, I., & Agnon, A. (2016). Large geomagnetic field anomalies revealed in Bronze to Iron Age archeomagnetic data from tel Megiddo and tel Hazor, Israel. *Earth and Planetary Science Letters*, *442*, 173–185.
Stillinger, M. D., Feinberg, J. M., & Frahm, E. (2015). Refining the archaeomagnetic dating curve for the Near East: New intensity data from Bronze Age ceramics at Tell Mozan, Syria. *Journal of Archaeological Science*, *53*, 345–355.

Stillinger, M. D., Hardin, J. W., Feinberg, J. M., & Blakely, J. A. (2016). Archeomagnetism as a Complementary dating technique to address the Iron Age chronology debate in the Levant. *Near East Archaeology*, *79*(2), 90–106.
Tauxe, L., Shaar, R., Jonestrask, L., Swanson-Hysell, N. L., Minnett, R., Koppers, A. A. P., et al. (2016). PmagPy: Software package for paleomagnetic data analysis and a bridge to the Magnetics information Consortium (MagIC) database. *Geochemistry, Geophysics, Geosystems*, *17*, 2450–2463.
Tauxe, L., & Staudigel, H. (2004). Strength of the geomagnetic field in the Cretaceous Normal Superchron: New data from submarine basaltic glass of the Troodos Ophiolite. *Geochemistry, Geophysics, Geosystems*, *5*(2). https://doi.org/10.1029/2003gc000635
Thellier, E., & Thellier, O. (1959). Sur l'intensité du champ magnétique terrestre dans le passé historique et géologique. *Annales de Geophysique*, *15*, 285–376.
Toffolo, M. B., Arie, E., Martin, M. A. S., Boaretto, E., & Finkelstein, I. (2014). Absolute chronology of Megiddo, Israel, in the late Bronze and Iron Ages: High-resolution radiocarbon dating. *Radiocarbon*, *56*(1), 221–244.
Ussishkin, D. (2018). *Megiddo-Armageddon: The story of the Canaanite and Israelite City*. Jerusalem: Israel Exploration Society.
Yadin, Y. (1972). *Hazor – The Head of All Those Kingdoms Joshua 11: 10 with a Chapter on Israelite Megiddo*. London, UK: British Academy.
Yu, Y., Tauxe, L., & Genevey, A. (2004). Toward an optimal geomagnetic field intensity determination technique. *Geochemistry, Geophysics, Geosystems*, *5*(2). https://doi.org/10.1029/2003gc000630
Zijderveld, J. D. A. (1967). AC demagnetization of rocks: Analysis of results. In D. W. Collinso, K. M. Creer, & S. M. Runcorn (Eds.), *Methods in Palaeomagnetism*. Amsterdam: Elsevier.

References From Supporting Information

Hussain, A. G. (1987). The secular variation of the geomagnetic-field in Egypt in the last 5000 years. *Pure and Applied Geophysics*, *125*(1), 67–90.
Nachasova, I. E., & Burakov, K. S. (1998). Geomagnetic variations in the VI-V millenia B.C. *Geomagnetism and Aeronomy*, *38*(4), 502–505.
Segal, Y. (2003). *Paleomagnetic secular variation of the last 4 Millennia recorded in Dead Sea Sediments and Archeological sites in Israel* (MSc thesis). Tel Aviv: Tel Aviv University.
Walton, D. (1986). Alteration and its effects on the reproducibility of archaeomagnitudes from Tel-el-Amarna. *Journal of Geomagnetism and Geoelectricity*, *38*(12), 1349–1352.
Walton, D. (1990). The intensity of the geomagnetic-field in the eastern Mediterranean between 1600 Bc and Ad 400. *Journal of Geomagnetism and Geoelectricity*, *42*(8), 929–936.
Yutsis-Akimova, S., Gallet, Y., & Amirov, S. (2018a). Rapid geomagnetic field intensity variations in the Near East during the 6th millennium BC: New archeointensity data from Halafian site Yarim Tepe II (Northern Iraq). *Earth and Planetary Science Letters*, *482*, 201–212.
Yutsis-Akimova, S., Gallet, Y., Petrova, N., Nowak, S., & Le Goff, M. (2018b). Geomagnetic field in the Near East at the beginning of the 6th millennium BC: Evidence for alternating weak and strong intensity variations. *Physics of the Earth and Planetary Interiors*, *282*, 49–59.